

Sulforaphane prevents and reverses allergic airways disease in mice via anti-inflammatory, antioxidant and epigenetic mechanisms

Simon Royce

Monash University

Paul Licciardi

Murdoch Children's Research Institute https://orcid.org/0000-0001-6086-6285

Raymond Beh

Monash University https://orcid.org/0000-0001-9801-1549

Jane Bourke

Monash University https://orcid.org/0000-0001-7314-9234

Mark Cooper

Monash University https://orcid.org/0000-0002-5953-642X

Chantal Donovan

Hunter Medical Research Institute, University of Newcastle

Andrew Hung

RMIT University

Ishant Khurana

Epigenetics in Human Health and Disease Laboratory, Department of Diabetes, Central Clinical School, Monash University, Melbourne

Julia Liang

Monash University https://orcid.org/0000-0002-3031-3169

Scott Maxwell

Monash University, Alfred Centre https://orcid.org/0000-0002-7801-0714

Nadia Mazarakis

Monash University https://orcid.org/0000-0001-7681-2775

Eleni Pitsillou

Monash University

Kenneth Snibson

University of Melbourne

Mark Tobin

Australian Synchrotron https://orcid.org/0000-0003-1862-0649

Katherine Ververis

Monash University

Jitraporn Vongsvivut

Australian Synchrotron

Mark Ziemann

Deakin University

Chrishan Samuel

Monash University https://orcid.org/0000-0003-0295-4214

Mimi Tang

Royal Children's Hospital https://orcid.org/0000-0002-3839-5293

Sam El-Osta

Monash University https://orcid.org/0000-0001-7968-7375

Tom Karagiannis (

tom.karagiannis@monash.edu)

Monash University https://orcid.org/0000-0002-9967-1546

Article

Keywords: sulforaphane, allergic airways disease, L-sulforaphane, epigenetic regulatory mechanisms

Posted Date: August 23rd, 2021

DOI: https://doi.org/10.21203/rs.3.rs-787983/v1

License: © • This work is licensed under a Creative Commons Attribution 4.0 International License.

Read Full License

- 1 Sulforaphane prevents and reverses allergic airways disease in mice via anti-inflammatory,
- 2 antioxidant and epigenetic mechanisms
- 3 Simon G. Royce^{1,2,3,4}, Paul V. Licciardi^{4,5}, Raymond C. Beh^{1,2}, Jane E. Bourke³, Mark E.
- 4 Cooper^{6,7}, Chantal Donovan^{8,9,10}, Andrew Hung¹¹, Ishant Khurana¹², Julia Liang^{1,11}, Scott
- 5 Maxwell¹², Nadia Mazarakis^{1,4,5,13}, Eleni Pitsillou^{1,11}, Kenneth J. Snibson¹³, Mark J. Tobin¹⁴,
- 6 Katherine Ververis^{1,2}, Jitraporn Vongsvivut¹⁴, Mark Ziemann^{12,15}, Chrishan S. Samuel¹⁶, Mimi
- 7 L.K Tang^{5,17,18}, Assam El-Osta¹² & Tom C. Karagiannis^{1,2,*}
- 8 1 Epigenomic Medicine Laboratory, Department of Diabetes, Central Clinical School, Monash
- 9 University, Alfred Centre, 99 Commercial Road, Melbourne, VIC, 3004, Australia
- 2 Department of Clinical Pathology, University of Melbourne, Parkville, VIC, 3010, Australia
- 3 Monash University, Department of Pharmacology, Biomedicine Discovery Institute, Clayton,
- 12 VIC, 3800, Australia
- 4 Infection and Immunity, Murdoch Children's Research Institute, Melbourne, VIC, 3052,
- 14 Australia
- 5 Department of Paediatrics, The University of Melbourne, Melbourne, VIC, 3010, Australia
- 6 Department of Diabetes, Central Clinical School, Monash University, Alfred Centre, 99
- 17 Commercial Road, Melbourne, VIC, 3004, Australia
- 7 Department of Endocrinology and Diabetes, The Alfred Hospital, Melbourne, VIC, 3004,
- 19 Australia
- 20 8 Priority Research Centre for Healthy Lungs, Hunter Medical Research Institute, University of
- 21 Newcastle, Newcastle, NSW, 2305, Australia
- 9 Centre for Inflammation, Centenary Institute, Camperdown, NSW, 2050, Australia
- 23 10 University of Technology Sydney, School of Life Sciences, Faculty of Science, Sydney,
- NSW, 2007, Australia
- 25 11 School of Science, STEM College, RMIT University, VIC, 3001, Australia
- 26 12 Epigenetics in Human Health and Disease Laboratory, Department of Diabetes, Central
- 27 Clinical School, Monash University, Alfred Centre, 99 Commercial Road, Melbourne, VIC,
- 28 3004. Australia
- 29 13 Faculty of Veterinary and Agricultural Sciences, University of Melbourne, Parkville, VIC,
- 30 3010, Australia
- 31 14 ANSTO-Australian Synchrotron, Clayton, VIC, 3168, Australia
- 32 15 School of Life and Environmental Sciences, Deakin University, Waurn Ponds, VIC, 3216,
- 33 Australia
- 34 16 Cardiovascular Disease Program, Monash Biomedicine Discovery Institute and Department
- of Pharmacology, Monash University, Clayton, VIC, 3800, Australia
- 36 17 Population Allergy Group, Murdoch Children's Research Institute, Parkville, VIC, 3052,
- 37 Australia
- 38 18 Department of Allergy and Immunology, Royal Children's Hospital, Parkville, VIC, 3052,
- 39 Australia
- 40 **Short title:** Sulforaphane attenuates allergic airways disease
- ***Author for correspondence:**
- 42 Tom Karagiannis, PhD
- 43 Head Epigenomic Medicine Program
- 44 Department of Diabetes, Central Clinical School, Monash University
- 45 Melbourne, VIC 3004, Australia
- 46 Email: tom.karagiannis@monash.edu; Phone number: +61 400 857 906

Abstract

1

2 Sulforaphane has been investigated in human pathologies and preclinical models of airway diseases. To provide further mechanistic insights, we explored L-sulforaphane (LSF) in the 3 ovalbumin (OVA)-induced chronic allergic airways murine model, with key hallmarks of 4 5 asthma. Histological analysis indicated that LSF prevented or reversed OVA-induced epithelial 6 thickening, collagen deposition, goblet cell metaplasia, and inflammation. Well-known antioxidant and anti-inflammatory mechanisms contribute to the beneficial effects of LSF. 7 8 Fourier transform infrared microspectroscopy revealed altered composition of macromolecules, including lipids, following OVA-sensitization, which were restored by LSF. RNA sequencing in 9 human peripheral blood mononuclear cells highlighted the anti-inflammatory signature of LSF. 10 Novel findings indicated that LSF reduced the expression and activity of histone deacetylase 8. 11 Further, LSF resulted in histone and α -tubulin hyperacetylation in vivo. More generally, this 12 13 study identified new epigenetic regulatory mechanisms accounting for the protective effects and 14 provide support for the potential clinical utility of LSF in allergic airways disease. 15 16 17

Introduction

16

17

18

19

20

21

22

23

1 2 Sulforaphane (SFN) is a dietary isothiocyanate released from the precursor glucoraphanin by the action of plant myrosinase or gut microbiota β-thioglucosidases ^{1, 2, 3}. Myrosinase hydrolyzes the 3 β-thioglucoside bond from glucosinolate substrates, producing glucose, sulfate, and an unstable 4 aglycone intermediate ^{4, 5}. The aglycone intermediate can be rearranged to form a number of 5 different products including isothiocyanates and nitriles ^{4, 5}. In addition to SFN, the myrosinase-6 dependent hydrolysis of glucoraphanin yields SFN-nitrile ⁴. Sulforaphane is metabolized through 7 the mercapturic acid pathway ⁶. The first step involves glutathione conjugation (SFN-GSH) 8 mediated by glutathione S-transferase (GST) enzymes ^{7,8}. Glutathione conjugates are cleaved 9 further to generate the cysteinylglycine conjugate (SFN-Cys-Gly), cysteine conjugate (SFN-10 Cys), and N-acetylcysteine conjugate (SFN-NAC), catalyzed by γ -glutamyltranspeptidase, 11 cysteinylglycinase, and *N*-acetyltransferase ^{7,8}. 12 13 Sulforaphane has been widely investigated in numerous human models of disease including 14 15

cancer chemoprevention, metabolic disorders, and neurological conditions ^{9, 10, 11}. Further, SFN has been studied in numerous preclinical and clinical models of lung damage and airway diseases ^{12, 13, 14, 15}. The lack of definitive findings from clinical studies to date, most likely reflects issues with extract preparations and dosage regimes ^{16, 17, 18}. A notable exception to this is the beneficial effects of SFN in airborne pollution studies ^{19, 20}. Mercapturic acids are detoxification products formed from GST-catalyzed reactions that are being used in clinical trials as biomarkers of exposure to environmental and industrial chemicals ^{19, 20, 21}. Sulforaphane has been shown to enhance the detoxification of toxic and carcinogenic airborne pollutants by increasing the elimination of mercapturic acids ^{19, 20}.

A multitude of mechanisms of action, predominantly involving activation of cellular antioxidant 2 3 and anti-inflammatory pathways, have been associated with the beneficial effects of SFN in 4 models of disease. It is well-known that SFN activates nuclear factor erythroid 2-related factor 2 5 (Nrf2) and in response to cellular stress, this transcription factor translocates into the nucleus and binds to the antioxidant response element (ARE) ^{18, 22}. The interaction of Nrf2 and coactivator 6 7 proteins with ARE results in the induction of phase II detoxification and antioxidant enzymes, such as heme oxygenase-1 (HO-1), NAD[P]H:quinone oxidoreductase-1 (NQO1), superoxide 8 dismutase (SOD), catalase (CAT), and glutathione (GSH) ²². Under basal conditions, Nrf2 is 9 sequestered in the cytosol by Kelch-like ECH-associated protein 1 (Keap1) ²². Recently it has 10 been shown that LSF causes a reduction of pro-inflammatory cytokine and chemokine 11 production, and alleviates inflammation by targeting antigen-presenting cells ²³. 12 13 Here, we investigated the effects of administration of L-sulforaphane (LSF) in a murine model of 14 ovalbumin (OVA)-induced chronic allergic airways disease (AAD). This model of chronic AAD 15 recapitulates several features of human asthma including airway inflammation, airway 16 remodeling and airway hyperresponsiveness (AHR) ^{24, 25, 26}. Apart from conventional histological 17 and immunohistological analyses we performed genome-wide mRNA-Seq to confirm the anti-18 19 inflammatory signature of LSF in human peripheral blood mononuclear cells (PBMC). Furthermore, we examined epigenetic mechanisms associated with LSF by investigating histone 20 deacetylase enzyme (HDAC) expression and histone acetylation status following LSF 21 administration both in vitro and in the animal model. 22

1 Results

2 Protective effects of L-sulforaphane in the ovalbumin-induced model of allergic airways

3 disease

7

9

10

11

12

13

14

15

16

4 We used the well-established OVA-induced chronic model of AAD to investigate protection and

5 reversal of pathological features associated with OVA-sensitization by LSF (Figs 1A, 1B and

6 2A). As a positive HDAC inhibitor control, we also explored the protective effects of the FDA

approved HDAC inhibitor suberoylanilide hydroxamic acid (SAHA) (Fig 1A) ²⁷. Using

8 hematoxylin and eosin (H&E) staining, we observed epithelial thickening, increased goblet cell

metaplasia and inflammatory cells peripheral to the bronchial epithelium and basement

membrane in sensitized and challenged mice (OVA-vehicle; OVA-VEH) (Fig 1C). The

membrane apoptotic marker, Annexin V, was used to assess for apoptosis in the bronchial

epithelium (Fig 1D), and morphometric analysis was used to examine epithelial (Fig 1E) and

subepithelial thickness (Fig 1F). These findings highlighted the effects of OVA-sensitization

and challenge in the OVA-VEH group compared to the saline control mice. LSF attenuated the

pathological features associated with OVA-VEH sensitization, whereas SAHA was not effective

in this model (Fig 1G).

17

18

20

21

22

L-sulforaphane reverses ovalbumin-induced allergic airways disease

19 Histological staining was performed to assess for structural changes including epithelial

thickness, goblet cell metaplasia and inflammatory infiltrate (Fig 2Bi). Similar to the prevention

model we observed goblet cell metaplasia and inflammatory cell infiltrate in the OVA-VEH

sensitized and challenged mice compared to saline control mice and mice treated with LSF. An

1 array of histological stains was performed to assess collagen and reticular fibers in the reversal

2 model (Fig 2B).

3

Masson's trichrome stain was used to highlight the overall change in collagen deposition and 4 changes to epithelial and subepithelial thickness highlighting the beneficial effects of LSF (Fig 5 2Bii). Silver impregnation of collagen and reticular fibers showed weak staining in the saline-6 and LSF-treated mice in comparison to the OVA-VEH group (Fig 2Biii). Gomori's aldehyde-7 8 fuchsin was used to highlight elastic fibers as seen in the fibers surrounding the blood vessels 9 (Fig 2Biv). We observed an increase in elastic fibers surrounding the inner and outer walls of the 10 smooth muscle in the OVA-VEH sensitized mice that was not present in the saline control or mice treated with LSF. Picrosirius red staining was used to show the differential changes in type 11 I and type III collagen deposition to determine the efficacy of LSF treatment in reducing the 12 deposition of type I collagen observed in sensitized airways (Fig 2Bv). Morphometric analysis of 13 Masson's trichrome-stained airways showed LSF significantly attenuated the increases in 14 epithelial thickness (Fig 2C) and subepithelial thickness (Fig 2D). Analysis of sirius red-stained 15 16 airways showed collagen type III deposition was not affected in the OVA-VEH sensitized mice (Fig 2E). In contrast, collagen type I was significantly increased following OVA-VEH 17 sensitization compared to saline control mice. Treatment of sensitized mice with LSF 18 19 significantly reduced the augmentation of collagen type I. To assess AHR, mice were challenged with nebulized methacholine (MCh), and the change in resistance from baseline was measured 20 by invasive plethysmography (Fig 2F). MCh-induced AHR was significantly elevated in OVA-21 22 VEH mice at doses above 12.5mg/ml MCh compared to saline mice. These effects were

significantly attenuated by LSF mice at doses above 25mg/ml MCh compared to the OVA-VEH

2 sensitized mice.

3

5

6

7

8

9

10

11

12

13

14

15

16

18

19

20

21

4 Molecular mechanisms associated with protection and reversal of ovalbumin-induced

allergic airways disease by L-sulforaphane

Immunohistochemical staining of α -smooth muscle actin (α -SMA) was used to identify

activation of the fibrotic pathway (Fig 3Ai). The results showed that α-SMA stained

myofibroblasts in the lamina propria was significantly elevated in the OVA-VEH sensitized mice

compared to saline control mice. Immunohistochemical images were quantitated to represent

myofibroblasts per 100µm of basement membrane length (Fig 3Aii). The increases in the

myofibroblasts observed in the OVA-VEH sensitized mice were significantly reduced by

treatment with LSF. Downregulation of the expression of Caveolin-1 in OVA-VEH sensitized

mice was evident by immunohistochemistry (Fig 3Bi). Analysis of the total area of Caveolin-1

expression highlights the significant decrease in OVA-VEH sensitized mice compared to the

saline controls and OVA-LSF treated mice (Fig 3Bii). We further assessed airway contraction to

MCh in precision cut lung slices from OVA-challenged mice exposed to LSF ex-vivo.

17 Representative traces measuring the percentage of the airway lumen from the initial area in lung

slices from the OVA-VEH mice showed bronchial contraction following perfusion of MCh at a

dose of 300nM (Fig 3C). Directly following a five-minute perfusion of MCh to induce airway

narrowing, LSF was perfused for the same period. Airway dilation was achieved after

approximately one minute of perfusion, in a concentration-dependent manner up to 15µM LSF

22 (Fig 3Ci) and 30µM LSF (Fig 3Cii).

Focal plane array-Fourier transform infrared (FPA-FTIR) microspectroscopy was used to 1 investigate changes in spatial distribution of the lipid compositions. As shown in the chemical 2 images (Fig 3Di), lung sections of the OVA-sensitized mouse presented higher intensities of 3 lipids in the bronchial epithelium, compared to those observed for the saline and OVA-LSF 4 mice. The average absorbance and second derivative spectra were calculated from spectra taken 5 6 from the bronchial epithelium (Figs 3Dii and 3Diii). The derivatization process, specifically 7 second derivatization, has been widely used in spectroscopic analysis because this mathematical 8 approach not only eliminates the baseline effect, but also allows accurate detection and positive 9 identification of band components that are hidden in the presence of broad overlapping spectral features. In this study, absorbance and second derivative spectra were used together for 10 comparing specific lipid bands in the high-wavenumber region. The main spectral features in the 11 high-wavenumber region include the broad v(O-H) stretching band centred at ~3285 cm⁻¹, and 12 v(CH₂/CH₃) stretching modes from methylene/methyl groups of lipids, which are presented as 13 triplet bands within 3000-2800 cm⁻¹ spectral range. By a comparison, the ν (O-H) stretching band 14 was shifted from 3290 cm⁻¹ in the saline-treated control mice, to 3292 and 3284 cm⁻¹ in the 15 OVA-VEH and OVA-LSF mice groups respectively, suggesting that OVA treatment caused an 16 alteration of intra- and intermolecular H-bonding in the lung tissue. There was no significant 17 18 peak shift observed for the v(CH₂/CH₃) stretching modes. However, the FPA-FTIR images of lipids clearly reveal changes in the intensity of these v(CH₂/CH₃) absorption peaks, showing a 19 20 decrease in lipid components in the OVA-LSF mice, and an increase of the lipid components in the OVA-VEH mice when compared with the saline group (Fig 3Di). 21

L-sulforaphane modulates key antioxidant defense pathways

22

- 1 To confirm LSF as an inducer of phase II detoxifying enzymes, immunofluorescence was used to
- 2 detect the presence of Nrf2 in the prevention and reversal models (Fig 4A). Strong staining of
- 3 Nrf2 was observed in both models in OVA-LSF treated mice. Analysis of the total fluorescence
- 4 (FL) and foci formation count highlighted significant increases on OVA-LSF treated mice in the
- 5 prevention (Figs 4Bi and 4Bii) and reversal model (Figs 4Biii and 4Biv). To investigate the
- 6 localization of Nrf2 foci, line scan analysis of 4',6-diamidino-2-phenylindole (DAPI) and Nrf2
- 7 staining patterns was performed (Fig 4C). Nrf2 was found in areas of strong DAPI staining
- 8 associated to heterochromatin in saline and OVA-VEH sensitized mice and elevated staining
- 9 sometimes outside of heterochromatic regions was seen in OVA-LSF treated mice. The
- 10 expression of the antioxidant superoxide dismutase 2 (SOD2) was assessed using
- immunohistochemistry in the reversal model and OVA-LSF reversed OVA-induced reduction in
- the expression levels (Fig 4D). Expression of heme oxygenase-1 (HO-1) was investigated via
- immunofluorescence in both models (Fig 4Ei). These findings indicated that LSF treatment of
- 14 OVA-sensitized mice could reverse the significant elevation seen in OVA-VEH mice in both the
- prevention (Fig 4Eii) and reversal models (Fig 4Eiii).
- 17 L-sulforaphane suppresses cytokine and chemokine secretion and downregulates pro-
- 18 inflammatory genes

- 19 Histologically (H&E)-stained lung sections were analyzed for inflammatory cell infiltrate. OVA-
- 20 sensitization resulted in a significant increase in inflammation compared to saline control mice.
- 21 In both models, LSF-treated mice had significantly lower inflammation scores compared with
- 22 OVA-VEH mice (Fig 5A).

2 We used immunohistochemistry to determine if LSF would affect the expression of pro-fibrotic 3 genes via the TGF-β/smad2 pathway. We showed LSF significantly increased Smad2 expression 4 compared to saline and OVA-VEH mice (Fig 5B). 5 6 We investigated cytokine and chemokine production from human PBMCs treated with or 7 without LSF (15µM, 30µM) and 10µM SAHA for 24 hours using a multiplex bead assay (Fig. 5C). We showed LSF at both concentrations (15µM, 30µM) significantly attenuated the 8 9 production of all cytokines and chemokines tested, while SAHA only significantly decreased the secretion of IL-1_B (Fig 5C). 10 11 To investigate whether these findings were reflected in the transcriptome, RNA-sequencing 12 13 libraries were constructed using total RNA obtained from PBMCs from healthy donors (n=4) following ex vivo treatment with or without 15µM LSF for 24 hours (Fig 5D). Differentially 14 expressed (DE) genes were determined using Deseq2 (n=4, LSF: no LSF) and subjected to gene 15 set enrichment analysis (GSEA) of GO gene sets, which were ranked by effect. Of the top 50 16 ranked gene sets shown (Fig 5Di), only six were upregulated, while 44 sets were downregulated. 17 18 We additionally filtered differential genes (FDR < 0.05) from the top 100 gene sets for key terms including chemokine, cytokine, immune and inflammation, all of which were predominately 19 downregulated and most notable for CCL and CXCL chemokines (Fig 5Dii). Genes encoding the 20 21 proteins investigated in Figs 5B and 5C are also highlighted as Selected Genes, which include:

23

22

TNF ($TNF\alpha$), SMAD2, IL6, IL1B ($IL-1\beta$), CXCL8 (IL-8) and CCL4 ($MIP-1\beta$).

1 L-sulforaphane preferentially binds to and inhibits histone deacetylase 8 and mediates

hyperacetylation of histone and non-histone proteins

2

23

3 To evaluate the epigenetic effects of LSF in airways, immunofluorescence was used to assess the 4 acetylation status of histones (H2B, H3 & H4) and non-histone protein α-tubulin (Figs 6A, B, and C). The findings indicated that LSF administration resulted in hyperacetylated histone H2B 5 6 in both the reversal and prevention models (Fig 6B) and hyperacetylated H3, H4 histones and α-7 tubulin in the reversal model (Fig 6C). Furthermore, we explored the expression of HDAC8 using immunofluorescence in the prevention model and the results show that HDAC8 expression 8 9 was significantly elevated in OVA-VEH sensitized mice compared to saline mice and OVA-LSF 10 treated mice (Fig 6D). To further explore the effects of LSF on HDAC8, direct enzymatic inhibition assays indicated LSF selectively inhibited HDAC8 activity (EC₅₀ = $92.07 \pm 7.45 \mu M$) 11 (Fig 6E). Immunoblot analysis of class I and class II HDAC enzyme expression in A549 lung 12 cells treated with or without 15µM LSF, further validated that LSF decreased HDAC8 13 14 expression, and increased acetylation of α -tubulin and histone H3 (Fig 6F). The broad spectrum HDAC inhibitor, SAHA (10µM) was used a positive control highlighting the comparatively 15 modest HDAC inhibitory effects of LSF. 16 17 We used the molecular docking program, AutoDock Vina, to propose energetically favorable 18 binding sites for LSF on the human class I HDACs: HDAC1, HDAC2, HDAC3 and HDAC8 ²⁸. 19 In particular, we sought to identify binding modes unique to HDAC8 that may explain its 20 21 susceptibility to inhibition by LSF compared to the other three members of the family. For docking to human HDAC8, we selected three structures that exemplified three distinct 22

conformations due to the flexible loop B residues S30-K36, adjacent to the catalytic zinc ²⁹.

These were named 1 pocket (loop B closed, resulting in a single, primary binding pocket, PDB 1 ID: 1T67); 2 pockets (loop B partially opened, with the presence of a secondary pocket adjacent 2 to the primary HDAC pocket, PDB ID: 1T64); and 1 groove (loop B fully opened, with the two 3 pockets merged, PDB ID: 1VKG) ²⁹. Alignment of these HDAC8 structures is shown in Figs 6Gi 4 and Gii, with loop B highlighted for comparison. For the 1 pocket (loop B closed) structure, 5 6 docking calculations predicted binding at the primary zinc pocket (Figs 6Giii and Giv) and at a 7 distant site, labelled external-1, both of which also existed in HDAC1-3. A novel site, labeled tertiary, was predicted to bind LSF to HDAC8, which was not predicted for HDAC1-3. This 8 9 pocket was enclosed by the helix-loop B-helix structural motif spanning residues 21-49, with LSF forming steric contacts with an aromatic cage of residues composed of W137, 141 and 315; 10 Y18 and 20; and a salt-bridge interaction between residue R37 and LSF (Fig 6Gv). Inspection of 11 the docking solutions for predicted LSF binding to other HDAC8 conformations revealed that a 12 number of sub-sites existed in the neighborhood of the novel tertiary site (Fig 6Gvi). Compared 13 14 to HDAC1-3, the loop B helix region of HDAC8 was shorter by two residues, as shown in the example sequence alignment between HDAC3 and 8 (Fig 6vii). This led to a wider pocket that 15 accommodated binding of LSF to the tertiary site of HDAC8, which was otherwise occluded by 16 17 the two extra residues as exemplified in HDAC3 (Fig 6Gvii). 18 19 Overall, our findings highlighted the protective effects of LSF in the OVA-induced model of 20 chronic AAD. Mechanisms involving antioxidant and anti-inflammatory pathways account for 21 the beneficial effects of LSF. LSF downregulated the expression and preferentially inhibited HDAC8. Furthermore, hyperacetylation of core histones and α -tubulin following administration 22

1 *in vivo* represented key epigenetic mechanisms associated with the effects of LSF in the model of

2 chronic AAD investigated (Fig 7).

3

4

Discussion

We examined the effects of LSF in the OVA-induced murine model of chronic AAD, and LSF 5 6 was found to prevent and reverse the pathological features associated with the model (Figs 1 and 7 2). The OVA-induced murine model is well characterized and recapitulates several hallmarks of chronic asthma ^{24, 26, 30}. Our findings highlighted that the key features associated with the model, 8 9 including epithelial thickening, goblet cell metaplasia, apoptosis in the bronchial epithelium, and inflammatory cell infiltration were prominent in OVA-VEH sensitized mice. In the reversal 10 model, LSF treatment significantly reduced the increase in collagen type I deposition and 11 connective tissue fibers that were observed in OVA-VEH sensitized mice (Fig 2). Likewise, LSF 12 significantly reduced the expression of α -SMA in myofibroblasts in the lamina propria, 13 attenuated the expression of Caveolin-1 induced by OVA, and significantly increased the 14 expression of phosphorylated Smad2 (Fig 5). In accordance with previous studies, our findings 15 16 indicated that LSF protected from MCh-induced increases in airway resistance both in vivo (Fig. 2), and *ex vivo* (Fig 3) ¹². 17

18

19

20

21

22

23

The antioxidant effects of LSF involving activation of phase II detoxification pathways have been widely investigated ¹². Additionally, the molecular mechanisms that mediate crosstalk between Nrf2 and nuclear factor kappa-light-chain-enhancer of activated B cells (NF-κB), which regulate oxidative stress and inflammation, have been explored ^{16, 17, 31}. Our findings demonstrated that LSF treatment resulted in the modulation of Nrf2 (Fig 4). A significant

- 1 increase in the overall expression of Nrf2 and Nrf2 foci was observed in OVA-LSF treated mice
- 2 and DAPI staining showed that Nrf2 was predominantly localized in heterochromatic regions
- 3 (Fig 4). This is in line with recent findings, which associated Nrf2 with DNA damage response
- 4 pathways highlighting the nuclear accumulation of Nrf2 and formation of foci at sites of DNA
- 5 damage ^{32, 33}.

- 7 An interesting finding was the significant overexpression of HO-1 in OVA-sensitized mice,
- 8 which was diminished by administration of LSF in both the prevention and reversal models (Fig.
- 9 4). Expression of HO-1 is significantly upregulated in response to a wide variety of stimuli
- 10 causing oxidative stress ³⁴. Investigation of the canonical pathway indicated that the expression
- of HO-1 was modulated by Nrf2. Our findings indicated that sensitization of mice with OVA
- resulted in the overexpression of HO-1, which was most likely independent of the Nrf2 pathway.
- A probable explanation was that OVA-sensitization created oxidative stress releasing stimuli that
- may have inhibited the transcriptional repressor BACH1, resulting in increased expression of
- HO-1 (Fig 4). It is understood that inhibition of BACH1 is sufficient for activation of HO-1
- irrespective of the status of Nrf2 ³⁴. This OVA-sensitization mediated overexpression of HO-1
- was consistent with previous findings in the context of asthma ³⁵. Therefore, we can assume that
- 18 LSF ameliorates oxidative stress stimuli induced by OVA, which cause the overexpression of
- 19 HO-1. Consistent with activation of the Nrf2 pathway, LSF elevated the expression of the major
- 20 detoxification enzyme SOD2, which was significantly diminished by OVA-sensitization
- compared to control mice (Fig 4).

- Our findings indicated reductions of inflammatory infiltrates in the *in vivo* model studied (Fig 5).
- 2 In human PBMC we showed significant reductions in pro-inflammatory cytokines and
- 3 chemokines following LSF treatment. This included IL-1β, IL-6, TNF-α, IL-8, IP-10, and MIP-
- 4 $1\beta^{23,36}$. We compared cytokine and chemokine release with the FDA approved pan-HDAC
- 5 inhibitor SAHA in PBMC cells ³⁷. Apart from IL-1β, there was no significant modulation of
- 6 other cytokine or chemokine secretion by SAHA at the concentration (10 μM) investigated (Fig.
- 5). Furthermore, in gene set enrichment analysis of RNA-Seq data in human PBMC, 44 gene sets
- 8 largely related to the immune response were downregulated and six gene sets were upregulated
- 9 following treatment with LSF. These findings were consistent in all four samples. Genes
- encoding for the expression of cytokines and chemokines such as *IL-6*, *IL-1A*, *IL-1B*, *EB13*,
- 11 CXCL5, and CXCL1, were primarily downregulated, highlighting the anti-inflammatory
- 12 signature of LSF ^{23, 36, 38}.

- A particularly interesting observation was the increase in lipid deposition in the bronchial
- epithelium of OVA-VEH sensitized mice, as indicated by FPA-FTIR chemical images and
- spectral analysis (Fig 3). Increased wall thickness has been shown to exacerbate airway
- 17 resistance and more recently, fat-associated airway remodeling has been identified as a potential
- 18 contributing factor ^{39, 40}. The relationship between adipose tissue within the airway wall and body
- mass index (BMI) in non-asthmatics versus asthmatics has been examined ³⁹. White adipose
- 20 tissue was present in the outer airway wall in all subject groups and was predominantly found in
- 21 large to medium sized airways ⁴⁰. Our FPA-FTIR data revealed that there was a significant
- 22 modulation of lipid components following LSF administration with lipid compositions in

1 airways resembling those of the control group, which was distinct from the OVA-VEH sensitized

2 mice (Fig 3).

3

6

7

8

10

11

12

13

14

15

16

4 Epigenetic mechanisms, predominantly chromatin modifications involving the acetylation-

5 deacetylation axis, have been implicated in numerous disease states including asthma and

chronic obstructive pulmonary disease 41, 42, 43, 44. One of the main mechanisms described is the

downregulation of the HDAC2 enzyme resulting in aberrant acetylation of the glucocorticoid

receptor and resistance to corticosteroid therapy ⁴⁵. This may call the potential clinical utility of

9 HDAC inhibitors in AAD into question. However, HDAC inhibitors have well-known

pleiotropic properties including modulating inflammatory and antioxidant pathways, and have

shown beneficial effects in numerous models of disease 46, 47, 48, 49, 50, 51. This includes studies

with the prototypical hydroxamic acid Trichostatin A and short-chain fatty acid, valproic acid, in

models of AAD ^{52, 53, 54, 55}. Here, unlike Trichostatin A, we show that the hydroxamic acid

HDAC inhibitor SAHA was not effective in modulating airway responses in our model, further

highlighting the complexities associated with the use of pleiotropic pan-HDAC inhibitors in

airways disease (Fig 1).

17

18

19

20

21

22

Our findings indicated that LSF modulated the acetylation of histones 2B and H3, and α -tubulin

in the mouse model studied (Fig 6). This, in accordance with previous work, has indicated that

SFN possesses HDAC inhibitor activity in vitro and in in vivo ^{56, 57, 58}. Using in vitro enzymatic

assays and in A549 human alveolar epithelial cells, we show that LSF preferentially inhibited the

HDAC8 enzyme with very modest activity in comparison to SAHA. As described, steric

- 1 hindrance may preclude relevant binding of LSF to other class I HDAC enzymes (Fig 6). Indeed,
- 2 we performed independent experiments using cell-free assays indicating that LSF did not inhibit
- any of the other metal-dependent HDAC enzymes at biologically relevant concentrations (mM
- 4 range for HDAC3, HDAC6, and HDAC7 and undetectable for others). This is an interesting
- observation as it has been previously shown that a potent specific HDAC8 inhibitor (PCI-34501),
- 6 attenuated airway responses in OVA-sensitized mice ⁵⁹.

- 8 A limitation of our study is that the potential effects of key SFN metabolites were not explicitly
- 9 investigated. We have recently shown that although not as potent as LSF, metabolites such as
- SFN-Cys and SFN-NAC, have important roles in anti-inflammatory pathways ²³. Here, we show
- acetylation of α -tubulin following *in vivo* administration of LSF (Fig 6). Given that acetylation
- of α -tubulin is regulated by inhibition of HDAC6, and our cell-free assays highlight that LSF
- preferentially inhibits HDAC8, it presumed that an LSF metabolite mediates this effect ⁶⁰.
- According to previous observations, the metabolite that most likely possesses HDAC inhibition
- activity is SFN-Cys ^{61, 62, 63}. Therefore, it is worthy to systematically investigate the biological
- 16 effects and bioactivity of SFN metabolites. However, these considerations do not detract from
- our findings which demonstrate accumulation of hyperacetylated histones and α -tubulin
- 18 following administration of LSF *in vivo* (Fig 6).

- 20 Overall, our findings confirmed the efficacy of LSF in attenuating pathologies associated with
- 21 AAD, involving activation of antioxidant and anti-inflammatory pathways (Fig 7). Preferential
- 22 inhibition of HDAC8 by LSF and accumulation of acetylated core histones and α -tubulin in vivo

- 1 following LSF administration represented a new epigenetic regulatory mechanism. Sulforaphane
- 2 and high glucoraphanin extracts have had mixed results in human trials and currently, there are
- 3 no therapeutic uses of SFN or extracts in the clinic. However, our findings along with
- 4 accumulated evidence, highlight the clinical potential of SFN as either a prophylactic or a
- 5 therapeutic in the context of AAD. A pharmaceutical grade stable form of LSF or optimized
- 6 glucoraphanin-rich extracts may enable clinical translation.

8

Materials and Methods

- 9 **Chemicals.** In animal studies, LSF (Santa Cruz Biotechnology, Dallas, Texas, USA) was used at
- a dose of 5mg/kg dissolved in 1% (v/v) dimethyl sulfoxide (DMSO, Sigma-Aldrich, St. Louis,
- MO, USA) in 0.9% (v/v) normal saline solution (Baxter Health Care, NSW, Australia) and
- SAHA (Sigma) was used at 100mg/kg in 1% (v/v) DMSO in 0.9% (v/v) saline. The selected
- doses are known to be biologically active and have been used in experimental murine models of
- disease without significant toxicity ^{64, 65}. Chemical structures of LSF and SAHA are shown in
- 15 Fig 1A. For *in vitro* studies, LSF, SAHA, and MCh were all purchased from Sigma. LSF, and
- SAHA were dissolved in 100% (v/v) DMSO and stored as stock solutions of 20mM (-80°C),
- 17 10mM (-20°C) and 1M (-80°C), respectively.

- 19 **Animals.** Six-week-old female BALB/c mice obtained from Walter and Eliza Hall Institute
- 20 Bioservices (prevention model; Parkville, VIC, Australia) and Monash Animal Services (reversal
- 21 model; Clayton, VIC, Australia). Mice were housed under specific pathogen-free conditions,
- 22 maintained at 21°C, 12-hour light/dark cycle, fed standard laboratory chow (Barastoc Stockfeeds,

1 Pakenham, VIC, Australia), and water *ad libitum*. The BALB/c mice strain was chosen for their

2 strong Th2 responses in OVA-induced AAD models ⁶⁶. Due to their increased sensitivity to

3 OVA and AAD models, female mice were chosen for this study ^{66, 67}. The prevention model

experimental protocol was approved by the Murdoch Children's Research Institute Animal

5 Ethics Committee (approval no. A597). The reversal model experimental protocol was approved

6 by the Monash University Animal Ethics Committee (MARP/2012/085). All mice were provided

an acclimatization period of 4–5 days before any experimentation. All experimental procedures

followed the Australian guidelines for the care and use of laboratory animals for scientific

purposes.

10

11

12

13

14

15

16

17

18

19

4

7

8

9

Mouse model of chronic allergic airways disease. To assess the effects of LSF in chronic AAD

two models were used to determine protective effects and ability to reverse AAD in an

established model of OVA-induced chronic AAD. This model was chosen for its pathological

similarities to human asthma, including increased allergic responses indicated by increased

immunoglobulin E against OVA (OVA-specific IgE), AHR and remodeling changes such as

epithelial remodeling, goblet cell metaplasia, and subepithelial collagen deposition (fibrosis).

Treatment groups were divided into the prevention and reversal models according to the

timelines shown in Figs 1B and 2A. Detailed protocols of the prevention model ⁵² and reversal

model ⁶⁸ have been described previously.

20

21

23

Prevention model. Briefly, mice were sensitized with two intraperitoneal (i.p) injections of 10μg

of grade V chicken egg OVA (Sigma) and 1mg of aluminum potassium sulphate adjuvant (alum)

(Sigma) in 0.5mL of 0.9% (v/v) saline, which was subsequently administered via i.p on days 0

- and 14. Mice were then challenged by whole body inhalation exposure (nebulization) to
- 2 aerosolized 2.5% (w/v) OVA in saline for 30 minutes, three days per week for six weeks using
- an ultrasonic nebulizer (NE-U07, Omron Corporation, Tokyo, Japan), between days 21 and 63 to
- 4 establish AAD. Following exposure to nebulized OVA, mice were treated with 5mg/kg LSF
- 5 (OVA-LSF) or 100mg/kg SAHA (OVA-SAHA, n=6) or vehicle control (OVA-VEH, n=15) by
- 6 i.p injection, three days per week for six weeks, which represent doses known to be effective and
- 7 non-toxic ^{30, 44}. A fourth group of mice were sensitized with 1mg alum in 0.5ml saline on days 0
- 8 and 14, and were challenged with saline aerosols three days per week for six weeks (n=15). Mice
- 9 were euthanized with an i.p injection of ketamine and xylazine (200 μg/g: 10 μg/g) 4 days after
- the last nebulization, on day 67.

12 **Reversal model**. Saline control mice (n=6) and vehicle control mice (OVA-VEH, n=6) were

- sensitized and nebulized to saline or OVA as described in the prevention model. Mice were
- treated with saline or 5mg/kg LSF (OVA-LSF, n=8) by i.p injection 24 hours after the last OVA
- nebulization five times every 72 hours between days 64 and 76. Mice were euthanized by i.p
- injection of ketamine and xylazine (200 μ g/g: 10 μ g/g) 48 hours after the last treatment on day
- 17 78.

18

- 19 **Measurement of airway reactivity in vivo.** AHR was assessed by plethysmography, 14 hours
- after the final treatment with LSF or vehicle using a mouse invasive plethysmograph (Buxco
- 21 Electronics, Troy, NY). Following anaesthetization using an i.p injection of ketamine and
- xylazine (200 μ g/g: 10 μ g/g), mice were tracheostomized and cannulated via the jugular vein.
- 23 Mice were ventilated with a small animal respirator (Harvard Apparatus, Holliston, MA)

delivering 0.01 ml/g bodyweight at a rate of 120 strokes/min. A baseline airway resistance was

2 recorded (Biosystem XA; Buxco Electronics), then every three minutes after increasing

3 intravenous doses of MCh (3.1, 6.3, 12.5, 25, 50 and 100 mg/ml) in phosphate buffered saline.

4 The change in airway resistance from baseline level per dose was recorded in Finepoint (Buxco

5 Electronics).

6

9

10

11

12

14

15

16

7 Measurement of airway reactivity ex vivo. Preparation of precision cut lung slices and

8 measurement of responses to MCh were performed in OVA-VEH sensitized mice as previously

described ^{69, 70}. Briefly, lungs were inflated with warm 2% (w/v) ultra-pure low melting point

agarose (Invitrogen, Carlsbad, CL, USA) in Hanks' balanced salt solution supplemented with 40

mM HEPES (HBSS, Sigma), via a tracheal cannula. After solidification of the agarose at 4°C (20

mins), a single lobe was mounted in cold HBSS to a vibratome (VT 1000S, Leica Microsystems,

Wetzler, Germany) in preparation for serial sectioning (150µm). Measurements of airway

responses to MCh was performed using a gravity-fed system where lung slices were perfused at

a constant rate (5 mins) for each condition; 300nM MCh, increasing doses of LSF (3, 10, 15 and

30μM) and HBSS in resting periods.

17

18

19

20

21

22

Lung histopathology. Lung tissues were dissected, and right lung lobes were fixed with 10%

(v/v) neutral buffered formalin (Sigma) for 24 hours, routinely processed and embedded in

paraffin. Lung sections (3µm) were assessed by standard histological staining procedures;

hematoxylin and eosin (H&E) for inflammatory cell infiltration, Masson's trichrome for

epithelial and subepithelial collagen deposition, silver impregnation for detection of reticular and

- 1 collagen fibers, Gomori's aldehyde-fuchsin for elastic fibers and sirius red staining for
- 2 differentiation of collagen type I and type III.

- 4 Airway tissue inflammation cell score. Airway inflammatory cell infiltration was determined
- 5 from H&E stained sections. A minimum of ten airways per mouse were captured using an
- 6 Olympus FSX100 microscope mounted with a digital camera (Olympus, Tokyo, Japan). The
- 7 degree of airway inflammatory cell infiltration around the bronchi was scored by two
- 8 independent blinded investigators using the following score scale: 0 = no inflammatory cells; 1 =
- 9 1-3 layers of inflammatory cells; 2 = 4-6 layers; 3 = 7-10 layers and congestion; or 4 = >10
- 10 layers of inflammatory cells and severe congestion. For each mouse, a minimum of ten airways
- were observed and the average scores were taken.

- Morphometric analysis of structural changes. Epithelial thickness and subepithelial collagen thickness were assessed from Masson's trichrome stained sections. A minimum of ten airways
- per mouse were captured using an Olympus FSX100 microscope mounted with a digital camera
- 16 (Olympus). Bronchi measuring between 150-350µm luminal diameter were analyzed using
- 17 Image Pro-Plus software (v6.0, Media Cybernetics, MD, USA) after calibration with a reference
- 18 micrometer slide. The thickness of the bronchial epithelial layer was measured by tracing around
- 19 the basement membrane and the luminal surface of epithelial, and calculating the mean distance
- between the two. Subepithelial collagen thickness was also measured by tracing around the outer
- extent of the total collagen layer in the submucosal region, around the basement membrane, and
- 22 the mean distance between these lines calculated. Differentiation of collagen type I and type III
- was assessed from sirius red F3B (Sigma) stained slides. Sirius red staining was captured under

- 1 polarized light using an Olympus BX61 microscope (Olympus) automated with a FVII digital
- 2 camera to differentiate between the types of collagen. Type I (red and yellow under polarized
- 3 light) and type III (green under polarized light) collagen was quantified using ImageJ analysis
- 4 software (FIJI v1.48a, NIH, Bethesda, MD).

- 6 Immunohistochemistry. Formalin-fixed paraffin embedded sections were used to evaluate the
- 7 protein expression of α -smooth muscle actin (α -SMA) to identify airway smooth muscle,
- 8 Caveolin-1, superoxide dismutase 2 (SOD2) and phosphorylated Smad2. Primary antibodies:
- 9 mouse monoclonal anti-αSMA (1:150, Dako, Glostrup, Denmark); rabbit polyclonal anti-
- 10 Caveolin-1 (1:1000, Santa Cruz Biotechnology); rabbit monoclonal (EPR2560Y) anti-SOD2
- 11 (1:250, Abcam, Cambridge, UK) and rabbit polyclonal anti-phospho-Smad2 (ser465/467)
- 12 (1:500, Cell Signaling Technology, Danvers, MA, USA) were bound, biotinylated and detected
- using streptavidin horseradish peroxidase (Dako). The chromogen 3,3-diaminobenzidine (DAB,
- 14 Thermo Fisher Scientific, Waltham, MA, USA) was used and sections were counterstained with
- 15 hematoxylin (Sigma). Images were acquired using the Olympus FSX100 microscope (Olympus),
- a minimum of five airways were collected per mouse. α -SMA was quantified by counting the
- number of myofibroblasts surrounding the airways per 100µm of basement membrane measured
- using Image Pro Plus Software (Media Cybernetics). All other antibodies were assessed by
- measuring the mean area (µm²) of the protein expressed by detecting DAB staining using Image
- J software (FIJI v1.48a, NIH, Bethesda, MD) incorporating the color deconvolution plugin,
- 21 which isolates the brown colour channel from the brightfield image.

- 1 **Immunofluorescence.** Formalin-fixed paraffin embedded sections were used to evaluate the
- 2 protein expression of: membrane apoptotic marker Annexin V; nuclear factor erythroid 2-related
- 3 factor 2 (Nrf2), which regulates antioxidant proteins like heme oxygenase-1 (HO-1); the
- 4 acetylated state of histones H2B (H2Bac), H3 (H3ac), H4 (H4ac) and non-histone protein α-
- 5 tubulin and histone deacetylase 8 (HDAC8) as previously described ⁵². Briefly, after
- 6 deparaffinization and antigen retrieval (Dako), slides were blocked using Superblock (Thermo
- 7 Fisher Scientific) and exposed to primary rabbit monoclonal antibodies: anti-Annexin V (1:500,
- 8 Abcam), anti-Nrf2 (1:250, Abcam), anti-HO-1 (1:500, Abcam), anti-histone H2B acetyl (K15)
- 9 (1:500, Abcam), anti-histone H3 acetyl (K9) (1:500, Abcam), rabbit polyclonal anti-histone H4
- acetyl (1:500, Millipore) and mouse monoclonal antibodies, anti-α-tubulin (1:500, Sigma) and
- anti-HDAC8 (1:250, Sigma) all diluted in 1% (v/v) bovine serum albumin (BSA, Sigma).
- 12 Primary antibodies were conjugated with secondary antibodies, goat anti-mouse Alexa 488
- 13 (Molecular Probes Invitrogen) and goat anti-rabbit 546 (Molecular Probes) diluted in 1% (v/v)
- 14 BSA (1:500) and mounted in Prolong Gold Antifade with DAPI (Invitrogen). Slides were
- incubated overnight at 4°C before imaging. Annexin V images were acquired using an Olympus
- 16 BX61 motorized upright fluorescence microscope automated with FVII Camera (Olympus) using
- a 10x/0.3 and 20x/0.5 U PLAN FL objectives and fluorescence filter cubes used included: DAPI
- 18 (λ_{ex} : 350/50, λ_{em} : 460/50nm), FITC (λ_{ex} : 470/40, λ_{em} : 525/50nm) and TRITC (λ_{ex} :545/30,
- 19 λ_{em} :620/60nm). All other antibodies were acquired using the Nikon A1R-si resonant scanning
- 20 confocal system with upright Nikon D-Eclipse microscope fitted with an automated digital
- 21 camera (Nikon Ti, Tokyo, Japan) in association with Nikon NIS-Elements AR 3.2 64-bit
- software (NIS Elements Advanced Research, Tokyo, Japan). Samples were captured using a
- 23 60x/1.0W DIC N2 ∞/0 oil 2.8 Nikon Japan NIR Apo oil immersion objective (NA=1.4). Images

- were acquired with sequential excitation: 405 nm (λ_{em} : 450/50), 488 nm (λ_{em} : 490/525) and 568 1
- nm (λ_{em} : 562/95) laser lines and collected in 512 x 512 pixel format (mono 16-bit) with a 0.5 μ m 2
- step size and 2.2 pixel/dwell. A minimum of five airways per mouse were acquired, and images 3
- were processed and analyzed for mean total fluorescence (FL) intensity using ImageJ (FIJI). 4
- Nrf2 foci and line scan analysis was assessed using Image J processing tools (FIJI). 5

- Focal plane array-Fourier transform infrared (FPA-FTIR) microspectroscopy. Lung 7
- samples were sectioned (4µm) using a Leica RM 2135 microtome (Leica Biosystems) onto 8
- calcium fluoride (CaF₂) windows (Crystran, Dorset, UK). The sections were subsequently 9
- deparaffinized by two consecutive 5 min washes with xylene (Sigma-Aldrich) and stored in 10
- 11 desiccator prior to FPA-FTIR microspectroscopy. The acquisition of FPA-FTIR chemical images
- was performed using an offline FPA-FTIR microspectroscopic system (Bruker Optik GmbH, 12
- Ettlingen, Germany) at the Australian Synchrotron Infrared Microspectroscopy (IRM) beamline 13
- (Clayton, VIC, Australia) as described previously ³⁰. Briefly, the FPA-FTIR images were 14
- acquired in transmission mode using a Bruker Hyperion 3000 FTIR microscope, with a liquid 15
- 16 nitrogen cooled 64 x 64 element FPA detector and a matching 15x objective and condenser (NA
- = 0.40), coupled to a Bruker Vertex 70 FTIR spectrometer with an internal thermal (GlobarTM) 17
- IR source. Each FPA-FTIR image (4 x 4 grid) was acquired within the 4,000–800 cm⁻¹ spectral 18
- region with a sampling area of 180 x 180μm². The spectral images were collected with 8 cm⁻¹ 19
- 20 resolution, 64 co-added scans, Blackman-Harris 3-term apodization, Power-Spectrum phase
- 21 correction, and a zero-filling factor of two, which were set as default acquisition parameters
- using the OPUS 7.2 imaging software suite (Bruker). Background spectra were measured using 22
- the same acquisition parameters, by focusing on a clean surface area of the CaF₂ window without 23

- any tissue. FPA-FTIR images were pre-processed for an atmospheric compensation, baseline
- 2 correction (concave rubberband algorithm) and vector normalization. The spatial distribution of
- 3 lipids were generated based on integrated areas under the lipid region (3,000-2,800 cm⁻¹).
- 4 Spectra localized to the bronchial epithelium (104 spectra for saline, 156 spectra for OVA-VEH
- 5 and 114 spectra for OVA-LSF airways) were extracted from the FPA-FTIR images. The
- 6 extracted spectra were then averaged and converted into its corresponding second derivative
- 7 using a 25 smoothing point Savitzky-Golay algorithm in OPUS 7.2 software (Bruker).

- 9 **HDAC8 activity profile.** To determine the *in vitro* HDAC inhibitor capacity of LSF against the
- metal-dependent HDAC1-11 enzymes, direct fluorescence based enzymatic inhibition assays
- were performed by Reaction Biology Corp. (Malvern, PA, USA) using the fluorogenic peptides
- from p53 residues 379-382 (RHKAcKAc), according to the company's standard operating
- procedures. Two independent experiments were performed and the EC_{50} values were determined
- from ten concentrations (0.01-100µM) assayed in three-fold serial dilution. SAHA was used as a
- reference compound. EC_{50} values were calculated by fitting the data to the four-parameter
- logistic equation using GraphPad Prism, v7.01 (GraphPad, San Diego, CA, USA).

- 18 **Cell culture for** *in vitro* **studies.** Human peripheral blood mononuclear cells (PBMC) were
- 19 fractionated using Ficoll Paque (GE Healthcare, Wauwatosa, Wisconsin, USA) from blood
- samples (healthy participants; n=4) obtained from the Australian Red Cross Blood Bank
- 21 (Melbourne, VIC, Australia) under ethics project (#304/12) approved by the Alfred Hospital
- 22 Ethics Committee (Alfred Health, Melbourne, VIC, Australia). Cells were harvested fresh on the

- day of experiments and maintained in complete-Roswell Park Memorial Institute (RPMI) 1640
- 2 medium supplemented with 20 mmol/L HEPES (pH 7.4; GIBCO-Invitrogen, Carlsbad, CA,
- 3 USA), 10% (v/v) fetal bovine serum (FBS, In vitro Technologies, Noble Park, VIC, Australia), 2
- 4 mmol/L L-glutamine (GIBCO-Invitrogen), and 1% (v/v) penicillin/streptomycin (GIBCO-
- 5 Invitrogen) at 37°C, 5% (v/v) CO₂. Human epithelial lung A549 cells, purchased from the
- 6 American Type Culture Collection (ATCC, Manassas, VA, USA), were grown as monolayers in
- 7 Dulbecco's Modified Eagle Medium (DMEM) (Life Technologies, Carlsbad, USA)
- 8 supplemented with 10% (v/v) FBS and 1% (v/v) penicillin/streptomycin and maintained in the
- 9 exponential growth phase under sterile conditions, 37°C, 5% (v/v) CO₂.
- 11 Chemokine and cytokine multiplex bead assay. Chemokines and cytokine production from
- mononuclear cells was measured by multiplex array. PBMCs were incubated with LSF (15μM
- and $30\mu\text{M}$), and SAHA ($10\mu\text{M}$) or left untreated for 24 hours at 37°C , 5% (v/v) CO₂.
- Supernatants were harvested following centrifugation (800g; 10 mins) and measured for the
- presence of IL-1β, IL-6, IL-8, IP-10, MIP-1β and TNF-α using the multiplex bead assay (Bio-
- Rad Laboratories Inc, Hercules, CA, USA) according to the manufacturers' procedures. All
- supernatants were assayed undiluted, in triplicate. Briefly, a standard curve was prepared using
- 18 four-fold serial dilutions of the cytokine standards provided using RPMI-FCS. Assay controls
- were prepared by adding known concentrations of the cytokine standard using a 1:2 and 1:4
- 20 dilution in RPMI-FCS. Culture medium was used as a negative control. Anti-cytokine beads and
- 21 matched anti-cytokine biotinylated reporters were measured on a Luminex 200 Bio-analyzer and
- data was analyzed in LuminexIS v2.3 software (Luminex Corporation, Austin, TX, USA), and
- concentrations reported in pg/ml.

23

2 RNA-Seq. PBMCs were cultured with or without 15µM LSF for 24 hours prior to RNA 3 extraction, which comprised of TRIzol (Invitrogen) cell lysis followed by RNeasy (Qiagen, 4 Hilden, Germany) column purification with on-column DNase treatment. Equal amounts of purified RNA (5mg per sample) were used in the construction of sequencing libraries (RNA-5 6 sequencing library preparation kit, Illumina, San Diego, CA, USA). Sequencing of RNA-Seq 7 libraries was performed on a Genome Analyzer IIx with a 36-cycle (v4) sequencing kit (Illumina). Sequence reads were extracted using Pipeline (v1.6) software (Illumina) before 8 9 alignment (GRCh38 cDNA reference, release-101, Ensembl) and quantification of transcript counts using Kallisto quant (v0.45.0) 71. Transcript level counts were aggregated to genes, before 10 sample normalization and differential expression analysis with Deseq2 (v1.28.1) ⁷². Differential 11 genes were ranked by significance and fold change as described previously ⁵¹, prior to gene set 12 enrichment analysis (GSEA) of gene ontology (GO) gene sets (v7.2) ⁷³, using 'mitch' (v1.0.8) ⁷⁴ 13 with mitch settings: priority='effect'. Heat maps and differential expression plots for RNA data 14 were generated using ggplot2 (v3.3.2) ⁷⁵. 15 16 Western blotting. To determine the effects of LSF on the expression of class I and II HDAC 17 enzymes, protein was assessed in A549 cells using immunoblotting techniques as previously 18 described ⁷⁶. Briefly, A549 cells were treated with 15µM LSF and 10µM SAHA for 24 hours 19 prior to cell lysis using mammalian protein extraction reagent (MPER, Thermo Fisher 20 21 Scientific). Protein was measured using the Bradford assay, fractionated using 4-12% Bis-Tris 22 SDS-PAGE (Invitrogen) and transferred to nitrocellulose membranes. The membranes were

incubated overnight with primary antibodies: polyclonal rabbit anti-HDAC1, HDAC2, HDAC3,

- 1 HDAC4, HDAC6, HDAC8, HDAC9 AND HDAC10 (2 μg/ml; BioVision Inc. Milpitas, CA,
- 2 USA), rabbit monoclonal anti-histone H3 acetyl (K9) (1 μg/ml, Abcam), mouse monoclonal anti-
- 3 α -tubulin (1 μ g/ml, Sigma) and mouse monoclonal anti-GAPDH (1 μ g/ml, Sigma). The
- 4 membranes were incubated with horseradish peroxidase-conjugated goat anti-mouse or donkey
- 5 anti-rabbit secondary antibodies (1:10000, Dako) followed by enhanced chemiluminescence
- 6 staining (Sigma).

- 8 **Molecular modeling.** AutoDock Vina ²⁸ was used to propose energetically favorable binding
- 9 sites for LSF on the human class I HDAC enzymes. For docking to human HDAC8, three
- structures from the RCSB Protein Data Bank (PDB) exemplifying three distinct conformations of
- HDAC8 co-crystallized with different inhibitors (PDB ID: 1T67, 1T64, 1VKG) were used ²⁹.
- Docking to HDAC2 and HDAC3 were performed on PDB ID: 3MAX and 4A69, respectively ^{77,}
- 13 ⁷⁸. For each HDAC structure, the first protein chain (chain A) was isolated, water molecules and
- other ligands were removed, and the zinc atom was retained for subsequent docking calculations.
- All HDAC structures were energy-minimized using GROMACS (v4.5.5) ⁷⁹ with the GROMOS
- 16 forcefield and 53A6 parameter set. Each HDAC structure was energy minimized using the
- steepest descent algorithm, and an energy gradient convergence criterion of 0.01 kcal/mol/Å.
- 18 The LSF structure was created using ChemDraw (Perkin Elmer, Waltham, MA, USA) and saved
- in PDB format. Docking calculations were performed using Autodock Vina. All HDAC and LSF
- 20 PDB files were processed using PyRx 80 to create their corresponding PDBQT files. All five
- 21 rotatable torsions for LSF were activated, while HDAC structures were assumed to be rigid.
- 22 PyRx was used to define the ligand search grid, identical for all HDACs modeled, with
- 23 dimensions x-size: 77, y-size: 65, and z-size: 60, encompassing the entire protein surface for an

1	exhaustive search of potential binding sites. The searches were conducted with an exhaustiveness
2	of 2000. The top 10 predicted LSF binding poses for each HDAC model were visualized and
3	analyzed using Visual Molecular Dynamics (v1.9.2) (VMD, Beckman Institute, Urbana, IL,
4	USA).
5	
6	Statistics. All data is expressed as mean \pm SEM, where each n represents a single mouse (> five
7	airways per mouse unless otherwise specified) or a single blood donor (n=4). Groups were
8	compared using a one-way analysis of variance (ANOVA) with a 95% confidence interval and
9	Tukey post-hoc test where appropriate using GraphPad Prism, v7.01 (GraphPad).
10	
11	
12	
12	
13	
14	
15	
16	
17	
18	
19	
20	

1 References

2 3 4	1.	Zhang Y, Talalay P, Cho CG, Posner GH. A major inducer of anticarcinogenic protective enzymes from broccoli: isolation and elucidation of structure. <i>Proceedings of the National Academy of Sciences of the United States of America</i> 89 , 2399-2403 (1992).
5 6 7 8	2.	Prochaska HJ, Santamaria AB, Talalay P. Rapid detection of inducers of enzymes that protect against carcinogens. <i>Proceedings of the National Academy of Sciences of the United States of America</i> 89 , 2394-2398 (1992).
9 10 11 12	3.	Fahey JW, Holtzclaw WD, Wehage SL, Wade KL, Stephenson KK, Talalay P. Sulforaphane bioavailability from glucoraphanin-rich broccoli: control by active endogenous myrosinase. <i>PloS one</i> 10 , e0140963-e0140963 (2015).
13 14 15	4.	Angelino D, <i>et al.</i> Myrosinase-dependent and –independent formation and control of isothiocyanate products of glucosinolate hydrolysis. <i>Front Plant Sci</i> 6 , (2015).
16 17 18 19	5.	Matusheski NV, Jeffery EH. Comparison of the bioactivity of two glucoraphanin hydrolysis products found in broccoli, sulforaphane and sulforaphane nitrile. <i>Journal of Agricultural and Food Chemistry</i> 49 , 5743-5749 (2001).
20 21 22 23	6.	Tortorella SM, Royce SG, Licciardi PV, Karagiannis TC. Dietary sulforaphane in cancer chemoprevention: the role of epigenetic regulation and HDAC inhibition. <i>Antioxidants & Redox Signaling</i> 22 , 1382-1424 (2015).
24 25 26	7.	Vanduchova A, Anzenbacher P, Anzenbacherova E. Isothiocyanate from broccoli, sulforaphane, and its properties. <i>Journal of Medicinal Food</i> 22 , 121-126 (2018).
27 28 29 30	8.	Amjad AI, Parikh RA, Appleman LJ, Hahm E-R, Singh K, Singh SV. Broccoli-derived sulforaphane and chemoprevention of prostate cancer: from bench to bedside. <i>Current Pharmacology Reports</i> 1 , 382-390 (2015).
31 32 33	9.	Zimmerman AW, <i>et al.</i> Randomized controlled trial of sulforaphane and metabolite discovery in children with Autism Spectrum Disorder. <i>Molecular Autism</i> 12 , 38 (2021).
34 35 36 37	10.	Sun Y, <i>et al.</i> Protective effects of sulforaphane on type 2 diabetes-induced cardiomyopathy via AMPK-mediated activation of lipid metabolic pathways and NRF2 function. <i>Metabolism - Clinical and Experimental</i> 102 , (2020).
38 39 40	11.	Singh K, <i>et al.</i> Sulforaphane treatment of autism spectrum disorder (ASD). <i>Proc Natl Acad Sci U S A</i> 111 , 15550-15555 (2014).
41		

1 2 3	12.	Brown RH, Reynolds C, Brooker A, Talalay P, Fahey JW. Sulforaphane improves the bronchoprotective response in asthmatics through Nrf2-mediated gene pathways. <i>Respiratory Research</i> 16 , 106 (2015).
4 5 6 7	13.	Jiao Z, Chang J, Li J, Nie D, Cui H, Guo D. Sulforaphane increases Nrf2 expression and protects alveolar epithelial cells against injury caused by cigarette smoke extract. <i>Molecular Medicine Reports</i> 16 , 1241-1247 (2017).
8 9 10 11	14.	Cho H-Y, <i>et al.</i> Sulforaphane enriched transcriptome of lung mitochondrial energy metabolism and provided pulmonary injury protection via Nrf2 in mice. <i>Toxicology and Applied Pharmacology</i> 364 , 29-44 (2019).
12 13 14 15	15.	Sudini K, et al. A randomized controlled trial of the effect of broccoli sprouts on antioxidant gene expression and airway inflammation in asthmatics. <i>The Journal of Allergy and Clinical Immunology In Practice</i> 4 , 932-940 (2016).
16 17 18 19	16.	Mazarakis N, Snibson K, Licciardi PV, Karagiannis TC. The potential use of l-sulforaphane for the treatment of chronic inflammatory diseases: A review of the clinical evidence. <i>Clinical Nutrition</i> 39 , 664-675 (2020).
20 21 22 23	17.	Houghton CA. Sulforaphane: its "coming of age" as a clinically relevant nutraceutical in the prevention and treatment of chronic disease. <i>Oxidative Medicine and Cellular Longevity</i> 2019 , 2716870-2716870 (2019).
24 25 26	18.	Fahey JW, Kensler TW. The challenges of designing and implementing clinical trials with broccoli sprouts and turning evidence into public health action. <i>Front Nutr</i> 8 , (2021).
27 28 29 30	19.	Kensler TW, <i>et al.</i> Modulation of the metabolism of airborne pollutants by glucoraphanin-rich and sulforaphane-rich broccoli sprout beverages in Qidong, China. <i>Carcinogenesis</i> 33 , 101-107 (2012).
31 32 33 34	20.	Egner PA, <i>et al.</i> Rapid and sustainable detoxication of airborne pollutants by broccoli sprout beverage: results of a randomized clinical trial in China. <i>Cancer prevention research</i> (<i>Philadelphia</i> , <i>Pa</i>) 7, 813-823 (2014).
35 36 37 38	21.	M. De Rooij Jan N. M. Commandeur Nico P. E. Vermeulen BEN. Mercapturic acids as biomarkers of exposure to electrophilic chemicals:applications to environmental and industrial chemicals. <i>Biomarkers</i> 3 , 239-303 (1998).
39 40 41	22.	Keum Y-S. Regulation of Nrf2-mediated phase II detoxification and anti-oxidant genes. <i>Biomolecules & Therapeutics</i> 20 , 144-151 (2012).
42 43 44	23.	Mazarakis N, <i>et al.</i> Examination of novel immunomodulatory effects of L-sulforaphane. <i>Nutrients</i> 13 , (2021).

1 2 3 4	24.	Royce SG, Patel KP, Samuel CS. Characterization of a novel model incorporating airway epithelial damage and related fibrosis to the pathogenesis of asthma. <i>Laboratory Investigation</i> 94 1326-1339 (2014).
5 6 7 8	25.	Casaro M, Souza VR, Oliveira FA, Ferreira CM. OVA-induced allergic airway inflammation mouse model. In: <i>Pre-Clinical Models: Techniques and Protocols</i> . (ed^(eds Guest PC). Springer New York (2019).
9 10 11	26.	Kim DI, Song M-K, Lee K. Comparison of asthma phenotypes in OVA-induced mice challenged via inhaled and intranasal routes. <i>BMC Pulmonary Medicine</i> 19 , 241 (2019).
12 13 14	27.	Bolden JE, Peart MJ, Johnstone RW. Anticancer activities of histone deacetylase inhibitors. <i>Nature Reviews Drug Discovery</i> 5 , 769-784 (2006).
L5 L6 L7	28.	Trott O, Olson AJ. AutoDock Vina: improving the speed and accuracy of docking with a new scoring function, efficient optimization, and multithreading. <i>J Comput Chem</i> 31 , 455-461 (2010).
18 19 20	29.	Somoza JR, et al. Structural snapshots of human HDAC8 provide insights into the class I histone deacetylases. Structure 12, 1325-1334 (2004).
21 22 23 24	30.	Mazarakis N, <i>et al.</i> Investigation of molecular mechanisms of experimental compounds in murino models of chronic allergic airways disease using synchrotron Fourier-transform infrared microspectroscopy. <i>Sci Rep</i> 10 , 11713 (2020).
25 26 27	31.	Wardyn JD, Ponsford AH, Sanderson CM. Dissecting molecular cross-talk between Nrf2 and NF κB response pathways. <i>Biochemical Society Transactions</i> 43 , 621-626 (2015).
28 29 30	32.	Sun X, et al. NRF2 preserves genomic integrity by facilitating ATR activation and G2 cell cycle arrest. <i>Nucleic Acids Research</i> 48 , (2020).
31 32 33	33.	Peng D, <i>et al.</i> NRF2 antioxidant response protects against acidic bile salts-induced oxidative stress and DNA damage in esophageal cells. <i>Cancer Letters</i> 458 , 46-55 (2019).
34 35 36	34.	Gozzelino R, Jeney V, Soares MP. Mechanisms of cell protection by heme oxygenase-1. <i>Annual Review of Pharmacology and Toxicology</i> 50 , 323-354 (2010).
37 38 39	35.	Kitada O, <i>et al.</i> Heme oxygenase-1 (HO-1) protein induction in a mouse model of asthma. <i>Clin Exp Allergy</i> 31 , 1470-1477 (2001).
10 11 12 13	36.	Al-Harbi NO, <i>et al.</i> Sulforaphane treatment reverses corticosteroid resistance in a mixed granulocytic mouse model of asthma by upregulation of antioxidants and attenuation of Th17 immune responses in the airways. <i>European Journal of Pharmacology</i> 855 , 276-284 (2019).

1 2 3	37.	Dokmanovic M, Clarke C, Marks PA. Histone deacetylase inhibitors: overview and perspectives <i>Molecular Cancer Research</i> 5 , 981 (2007).
4 5 6 7	38.	Starrett W, Blake DJ. Sulforaphane inhibits de novo synthesis of IL-8 and MCP-1 in human epithelial cells generated by cigarette smoke extract. <i>Journal of Immunotoxicology</i> 8 , 150-158 (2011).
8 9 10	39.	Elliot JG, Donovan GM, Wang KCW, Green FHY, James AL, Noble PB. Fatty airways: implications for obstructive disease. <i>European Respiratory Journal</i> 54 , 1900857 (2019).
11 12 13	40.	Higami Y, <i>et al.</i> Increased epicardial adipose tissue is associated with the airway dominant phenotype of chronic obstructive pulmonary disease. <i>PLos one</i> 11 , e0148794 (2016).
14 15 16	41.	Adcock IM, Tsaprouni L, Bhavsar P, Ito K. Epigenetic regulation of airway inflammation. <i>Curr Opin Immunol</i> 19 , 694-700 (2007).
17 18 19	42.	Royce SG, Karagiannis TC. Histone deacetylases and their role in asthma. <i>J Asthma</i> 49 , 121-128 (2012).
20 21 22	43.	Ito K, et al. Expression and activity of histone deacetylases in human asthmatic airways. Am J Respir Crit Care Med 166, 392-396 (2002).
23 24 25	44.	Khurana I, <i>et al.</i> SAHA attenuates Takotsubo-like myocardial injury by targeting an epigenetic Ac/Dc axis. <i>Signal Transduction and Targeted Therapy</i> 6 , 159 (2021).
26 27 28	45.	Barnes PJ. Mechanisms and resistance in glucocorticoid control of inflammation. <i>J Steroid Biochem Mol Biol</i> 120 , 76-85 (2010).
29 30	46.	Adcock IM. HDAC inhibitors as anti-inflammatory agents. <i>Br J Pharmacol</i> 150 , 829-831 (2007)
31 32 33	47.	Xu WS, Parmigiani RB, Marks PA. Histone deacetylase inhibitors: molecular mechanisms of action. <i>Oncogene</i> 26 , 5541-5552 (2007).
34 35 36	48.	Karagiannis TC, El-Osta A. Will broad-spectrum histone deacetylase inhibitors be superseded by more specific compounds? <i>Leukemia</i> 21 , 61-65 (2007).
37 38 39	49.	Lunke S, <i>et al</i> . Epigenetic evidence of an Ac/Dc axis by VPA and SAHA. <i>Clinical Epigenetics</i> 13 , 58 (2021).
40 41 42	50.	Pirola L, <i>et al</i> . Genome-wide analysis distinguishes hyperglycemia regulated epigenetic signatures of primary vascular cells. <i>Genome Research</i> 21 , 1601-1615 (2011).

1 2 3	51.	Rafehi H, <i>et al.</i> Vascular histone deacetylation by pharmacological HDAC inhibition. <i>Genome Res</i> 24 , 1271-1284 (2014).
4 5 6 7	52.	Royce SG, <i>et al.</i> Protective effects of valproic acid against airway hyperresponsiveness and airway remodeling in a mouse model of allergic airways disease. <i>Epigenetics</i> 6 , 1463-1470 (2011).
8 9 10	53.	Royce SG, <i>et al.</i> Effects of the histone deacetylase inhibitor, trichostatin A, in a chronic allergic airways disease model in mice. <i>Arch Immunol Ther Exp (Warsz)</i> 60 , 295-306 (2012).
11 12 13	54.	Choi JH, Oh SW, Kang MS, Kwon HJ, Oh GT, Kim DY. Trichostatin A attenuates airway inflammation in mouse asthma model. <i>Clin Exp Allergy</i> 35 , 89-96 (2005).
14 15 16	55.	Ren Y, <i>et al.</i> Therapeutic effects of histone deacetylase inhibitors in a murine asthma model. <i>Inflamm Res</i> 65 , 995-1008 (2016).
17 18 19	56.	Ho E, Clarke JD, Dashwood RH. Dietary sulforaphane, a histone deacetylase inhibitor for cancer prevention. <i>J Nutr</i> 139 , 2393-2396 (2009).
20 21 22 23	57.	Myzak MC, Tong P, Dashwood WM, Dashwood RH, Ho E. Sulforaphane retards the growth of human PC-3 xenografts and inhibits HDAC activity in human subjects. <i>Exp Biol Med (Maywood)</i> 232 , 227-234 (2007).
24 25 26	58.	Myzak MC, Ho E, Dashwood RH. Dietary agents as histone deacetylase inhibitors. <i>Mol Carcinos</i> 45 , 443-446 (2006).
27 28 29 30	59.	Li ML, Su XM, Ren Y, Zhao X, Kong LF, Kang J. HDAC8 inhibitor attenuates airway responses to antigen stimulus through synchronously suppressing galectin-3 expression and reducing macrophage-2 polarization. <i>Respir Res</i> 21 , 62 (2020).
31 32	60.	Hubbert C, et al. HDAC6 is a microtubule-associated deacetylase. <i>Nature</i> 417 , 455-458 (2002).
33 34 35 36	61.	Nian H, Delage B, Ho E, Dashwood RH. Modulation of histone deacetylase activity by dietary isothiocyanates and allyl sulfides: studies with sulforaphane and garlic organosulfur compounds. <i>Environ Mol Mutagen</i> 50 , 213-221 (2009).
37 38 39	62.	Dashwood RH, Myzak MC, Ho E. Dietary HDAC inhibitors: time to rethink weak ligands in cancer chemoprevention? <i>Carcinogenesis</i> 27 , 344-349 (2006).
40 41 42 43	63.	Myzak MC, Dashwood RH. Histone deacetylases as targets for dietary cancer preventive agents: lessons learned with butyrate, diallyl disulfide, and sulforaphane. <i>Curr Drug Targets</i> 7 , 443-452 (2006).

1 2 3 4	64.	Wu W, Peng G, Yang F, Zhang Y, Mu Z, Han X. Sulforaphane has a therapeutic effect in an atopic dermatitis murine model and activates the Nrf2/HO1 axis. <i>Mol Med Rep</i> 20 , 1761-1771 (2019).
5 6 7 8	65.	Yan B, <i>et al.</i> Sulforaphane prevents bleomycin-induced pulmonary fibrosis in mice by inhibiting oxidative stress via nuclear factor erythroid 2-related factor-2 activation. <i>Mol Med Rep</i> 15 , 4005-4014 (2017).
9 10 11	66.	Melgert BN, <i>et al</i> . Female mice are more susceptible to the development of allergic airway inflammation than male mice. <i>Clin Exp Allergy</i> 35 , 1496-1503 (2005).
12 13 14	67.	Hayashi T, Adachi Y, Hasegawa K, Morimoto M. Less sensitivity for late airway inflammation in males than females in BALB/c mice. <i>Scand J Immunol</i> 57 , 562-567 (2003).
15 16 17 18	68.	Royce SG, Miao YR, Lee M, Samuel CS, Tregear GW, Tang ML. Relaxin reverses airway remodeling and airway dysfunction in allergic airways disease. <i>Endocrinology</i> 150 , 2692-2699 (2009).
19 20 21	69.	Donovan C, et al. Differential effects of allergen challenge on large and small airway reactivity in mice. PLoS One 8, e74101 (2013).
22 23 24	70.	Donovan C, Royce SG, Vlahos R, Bourke JE. Lipopolysaccharide does not alter small airway reactivity in mouse lung slices. <i>PLoS One</i> 10 , e0122069 (2015).
25 26 27	71.	Bray NL, Pimentel H, Melsted P, Pachter L. Near-optimal probabilistic RNA-seq quantification. <i>Nat Biotechnol</i> 34 , 525-527 (2016).
28 29 30	72.	Love MI, Huber W, Anders S. Moderated estimation of fold change and dispersion for RNA-seq data with DESeq2. <i>Genome Biol</i> 15 , 550 (2014).
31 32 33	73.	Mootha VK, <i>et al.</i> PGC-1alpha-responsive genes involved in oxidative phosphorylation are coordinately downregulated in human diabetes. <i>Nat Genet</i> 34 , 267-273 (2003).
34 35 36	74.	Kaspi A, Ziemann M. mitch: multi-contrast pathway enrichment for multi-omics and single-cell profiling data. <i>BMC Genomics</i> 21 , 447 (2020).
37 38	75.	Wickham HD. ggplot2: Elegant Graphics for Data Analysis. Springer-Verlag (2016).
39 40 41 42	76.	Ververis K, Karagiannis TC. An atlas of histone deacetylase expression in breast cancer: fluorescence methodology for comparative semi-quantitative analysis. <i>Am J Transl Res</i> 4 , 24-43 (2012).
43		

1 2	77.	Bressi JC, <i>et al.</i> Exploration of the HDAC2 foot pocket: Synthesis and SAR of substituted N-(2-aminophenyl)benzamides. <i>Bioorganic & Medicinal Chemistry Letters</i> 20 , 3142-3145 (2010).
3 4 5	78.	Watson PJ, Fairall L, Santos GM, Schwabe JWR. Structure of HDAC3 bound to co-repressor and inositol tetraphosphate. <i>Nature</i> 481 , 335-340 (2012).
6 7	79.	Lindahl A, Hess, & van der Spoel. GROMACS 2020.4 Manual. (ed^(eds Zenodo.) (2020).
8 9 10	80.	Dallakyan S. OAJ. <i>Small-molecule library screening by docking with PyRx</i> . Humana Press (2015).
11		
12		
13		
14		
15		
16		
17		
18		
19		
20		
21		
22		
23		
24		
25		

1 Figure Legends

23

Figure 1. L-sulforaphane protects from bronchial mucosal damage in a murine chronic 2 model of allergic airways disease. Chemical structures of antioxidant isothiocyanate, L-3 sulforaphane (LSF), and broad-spectrum histone deacetylase inhibitor suberoylanilide 4 hydroxamic acid (SAHA) (A), used in this study. The ovalbumin (OVA)-induced chronic murine 5 6 model of allergic airway disease (AAD) was investigated (B). Hematoxylin and eosin (H&E) 7 stained sections of formalin-fixed paraffin-embedded mouse lung tissue derived from the prevention model show LSF attenuates epithelial thickening induced by OVA. Little or no 8 9 peribronchial inflammatory infiltrate was observed for the saline and OVA-LSF mice, while severe to moderate peribronchial inflammatory infiltrate was present in the OVA-vehicle (OVA-10 VEH) and OVA-SAHA mice respectively (C). Immunofluorescence staining of Annexin V (red), 11 a membrane apoptotic marker and histone deacetylase enzyme (HDAC) 8 (green) (D). Strong 12 staining of Annexin V was found in the bronchial epithelium and peribronchial inflammatory 13 14 cells in mice treated with OVA-VEH and OVA-SAHA. Weak Annexin V staining was observed in the OVA-LSF mice and no staining was found in the epithelium of the control saline group. 15 Merged image: nucleus stained with 4',6-diamidino-2-phenylindole (DAPI) (blue), Annexin V 16 17 (red), HDAC8 (green). Morphometric analysis of epithelial thickness (E) and subepithelial collagen (F) from H&E stained lung sections shows both OVA-VEH and OVA-SAHA mice 18 19 significantly elevated epithelial and subepithelial thickness compared to saline and OVA-LSF 20 mice. Image J analysis of the mean fluorescence intensity of Annexin V expression showed 21 significantly elevated expression in OVA-VEH and OVA-SAHA mice compared to saline and 22 OVA-LSF mice. Data shown as the mean \pm SEM; **p<0.01 and ***p<0.001.

Figure 2. L-sulforaphane reverses bronchial remodeling in a murine model of chronic 1 allergic airways disease. In the reversal model, L-sulforaphane (LSF) was administered 2 3 following ovalbumin (OVA) sensitization (A). Representative photomicrographs of histological stained sections of formalin-fixed paraffin-embedded mouse lung tissue derived from the 4 reversal model (B). Hematoxylin and eosin (H&E) staining shows LSF reduces peribronchial 5 6 inflammatory cell infiltrate induced by OVA (Bi). Masson's trichrome staining shows a thin 7 epithelium (arrow) and little subepithelial collagen (arrowhead) in the saline and OVA-LSF mice 8 (Bii). Airways in OVA-vehicle (OVA-VEH) mice display epithelial thickening (arrow) and 9 severe subepithelial collagen deposition (arrowhead). Silver impregnation staining highlights that LSF attenuates the increased reticular fibers (R) and collagen fibers (C) found in the OVA-VEH 10 mice (Biii). Gomori's aldehyde-fuchsin staining shows an increase of elastic fibers (royal blue) 11 surrounding the inner and outer walls of the smooth muscle in the OVA-VEH mice that is not 12 present in the saline and OVA-LSF mice (Biv). Blood vessels (BV) stained positive. Sirius red 13 14 staining imaged under polarized light differentiates between collagen type I (red/yellow) and type III (green) in lung sections (Bv). Morphometric analysis of Masson's trichrome stained 15 sections shows OVA-VEH had significantly elevated epithelial thickness (C) and subepithelial 16 17 collagen thickness (D) when compared to both saline and OVA-LSF mice. Analysis of type I and III collagen from sirius red stained sections indicates that OVA-VEH significantly elevates type I 18 19 collagen when compared to all other groups (E). Airway hyperresponsiveness to methacholine 20 was recorded using plethysmography 48 hours following the final treatment and nebulization (F). 21 Increasing doses of methacholine was administered and maximal resistance values (cmH₂O/mL/sec) after 5 min was recorded. OVA-VEH mice had elevated airway resistance at 22

the highest methacholine dose as compared to saline mice. OVA-LSF mice had significantly

- 1 lower airway resistance at the highest methacholine dose compared to those of OVA-VEH mice.
- All data represented as the mean \pm SEM; *p<0.05 **p<0.01 and ***p<0.001.

- 4 Figure 3. Molecular effects of L-sulforaphane in the chronic allergic airways disease model.
- 5 Immunohistochemistry was performed on formalin-fixed paraffin-embedded mouse lung tissue
- derived from the reversal model. Representative photomicrographs of α -smooth muscle actin (α -
- 7 SMA) expression (Ai) and immunohistochemical morphometric analysis (Aii) shows staining for
- 8 α -SMA in the myofibroblasts in the lamina propria was significantly elevated in ovalbumin-
- 9 vehicle (OVA-VEH) mice compared to saline and ovalbumin-L-sulforaphane (OVA-LSF) mice.
- LSF significantly attenuated the reduced expression of Caveolin-1 following OVA-sensitization
- in OVA-VEH mice as observed by immunohistochemical images of Caveolin-1 (Bi) and
- morphometric analysis in bronchial epithelium (Bii). Data shown as the mean \pm SEM; *p<0.05
- and ***p<0.001. The comparison of small airway responses to methacholine (MCh) in precision
- cut lung slices from OVA-VEH mice (C). Representative traces show bronchial constriction as a
- percent of the initial lumen area in response to 300nM MCh and subsequent bronchial dilation
- 16 following a step-wise increase in concentrations of LSF to a maximum of 15µM (Ci) and 30µM
- 17 (Cii). Focal plane array-Fourier-transform infrared spectroscopy (FPA-FTIR) chemical images of
- lipid distributions of lung sections derived from the reversal model (Di). Average absorbance
- spectra (obtained from >100 individual spectra) from the bronchial epithelium (Dii) and their
- 20 corresponding second derivative spectra (Diii) highlight key changes in spectral patterns in lipid
- 21 regions.

- 1 Figure 4. L-sulforaphane modulates key antioxidant defense pathways in both the
- 2 prevention and reversal model of chronic allergic airways disease. Representative
- 3 immunofluorescent photomicrographs of lung sections stained with nuclear factor erythroid 2-
- 4 related factor 2 (Nrf2) (red) show strong staining in ovalbumin-L-sulforaphane (OVA-LSF) mice
- 5 in both the prevention and reversal model (A). Merged image: nucleus stained with 4',6-
- 6 diamidino-2-phenylindole (DAPI) (blue), Nrf2 (red). Nrf2 was analyzed using Image J for mean
- 7 fluorescence (FL) intensity (Bi, iii), number of focal points (Bii, iv) and co-localization to DAPI
- 8 staining (C). Nrf2 expression was significantly elevated in both the prevention (Bi) and reversal
- 9 (Biii) models, and the number of foci also significantly increased in the prevention (Bii) and
- 10 reversal (Biv) models. Line scan analysis indicated that Nrf2 expression co-
- localizes predominantly with heterochromatin according to DAPI staining in both saline and
- 12 OVA-vehicle (OVA-VEH) mice lung sections. Nrf2 was sometimes found outside
- 13 heterochromatic regions in OVA-LSF mouse lungs (C). Immunohistochemical images of
- superoxide dismutase 2 (SOD2) in paraffin-embedded mouse lung tissue derived from the
- reversal model (Di). Morphometric analysis showed a significant elevation of SOD2 protein
- expression in the bronchial epithelium in OVA-LSF mice compared to OVA-VEH mice (Dii).
- 17 Immunofluorescence photomicrographs of lung sections stained with heme oxygenase-1 (HO-1)
- 18 (red) and DAPI (blue) in the reversal model of allergic airways disease (AAD) (Ei). Analysis of
- the mean FL intensity of HO-1 showed significant elevation of HO-1 expression in the OVA-
- VEH mice in both the prevention (Eii) and reversal (Eiii) models. OVA-LSF treatment
- 21 significantly decreased the HO-1 elevation in both models. All data represented as the mean \pm
- 22 SEM; *p<0.05 **p<0.01 and ***p<0.001.

- 1 Figure 5. L-sulforaphane reduces inflammation via down-regulation of pro-inflammatory
- 2 **genes.** Ovalbumin-L-sulforaphane (OVA-LSF) significantly attenuates inflammation observed in
- 3 the ovalbumin-vehicle (OVA-VEH) mice in both the prevention and reversal model
- 4 (A). Inflammatory cell infiltration of hematoxylin and eosin stained sections of mouse airways
- was scored by two independent blinded investigators using the scale: 0 = no inflammation; 1 = 3
- layers of inflammatory cells; 2 = 6 layers; 3 = 10 layers and congestion; or 4 = 10 layers of
- 7 inflammatory cells and severe congestion. Representative immunohistochemical
- 8 photomicrographs detecting phosphorylated Smad2 (Bi) performed on formalin-fixed paraffin-
- 9 embedded mouse lung tissue derived from the reversal model. Morphometric analysis of stained
- sections shows OVA-LSF mice had a significant increase of phosphorylated
- Smad2 (Bii) expression compared to the saline and OVA-VEH mice. The anti-inflammatory
- effect of LSF was explored in peripheral blood mononuclear cells (PMBC) from healthy adults
- 13 (n=4). PBMCs were treated with the indicated concentrations of LSF and 10µM of
- suberoylanilide hydroxamic acid (SAHA) (C), the chromatin modifying control compound. An
- array of chemokines and cytokines were measured by the multiplex bead array assay as
- indicated. All data is represented as the mean \pm SEM; *p<0.05 **p<0.01 and ***p<0.001. RNA-
- 17 Seq was performed on adult PBMCs cultured with or without 15µM LSF for 24 hours.
- 18 Differentially expressed (DE) genes were subjected to gene set enrichment analysis (GSEA) of
- 19 gene ontology (GO) gene sets and examined for effect (D). Heat map of the top 50 gene sets
- 20 according to effect demonstrates predominate downregulation of sets related to immune response
- 21 (Di). The sets as shown are ordered by GSEA enrichment score according to analysis of
- 22 combined DE genes n=4 (first column); individual sample data is also shown (columns 2 to 5).
- 23 Heat map color gradient indicates GSEA enrichment score. Differential expression of genes

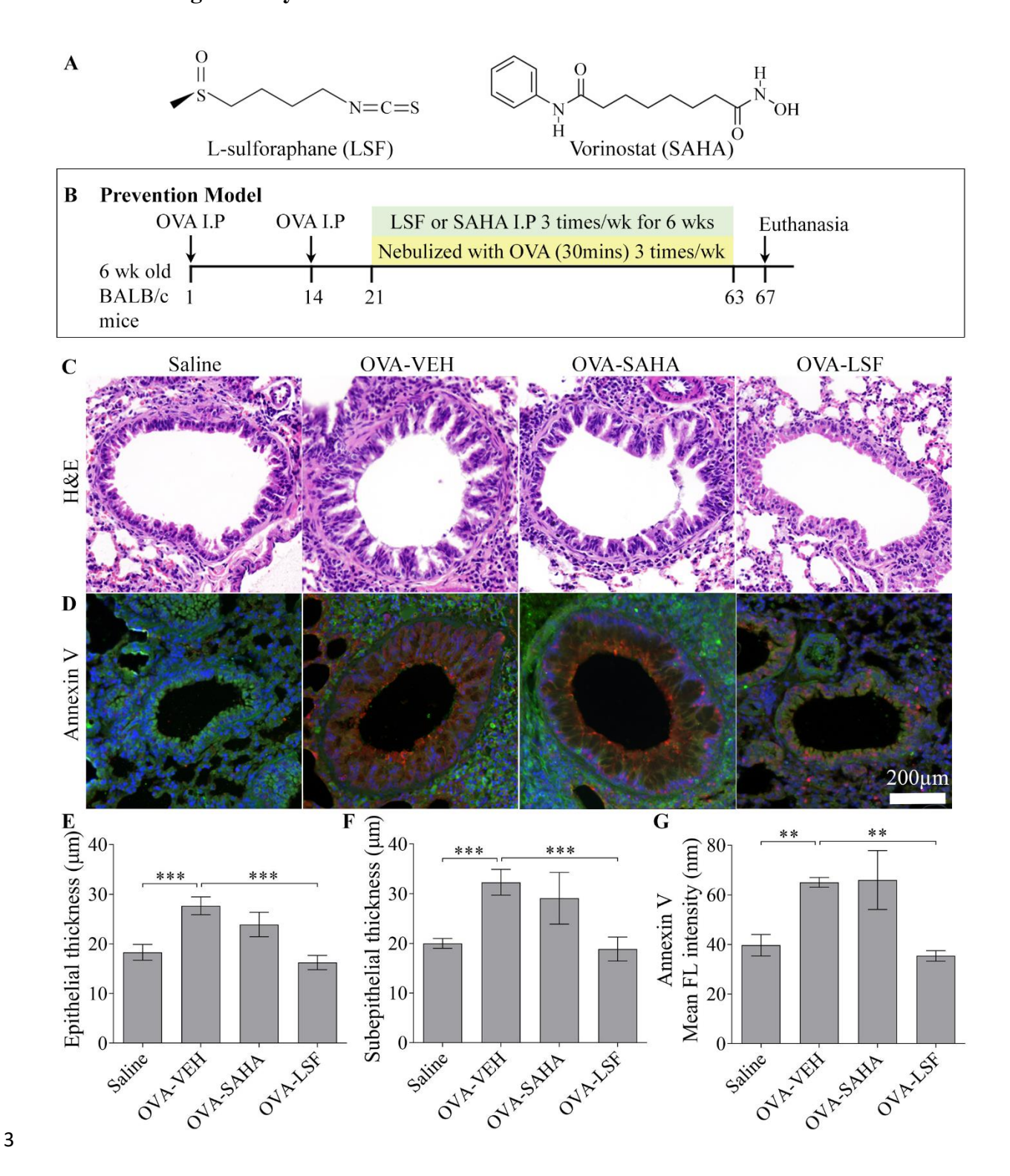
- from selected gene sets (Dii). Genes from the top 100 gene sets ranked by effect were filtered for
- 2 key terms including chemokine, cytokine, immune and inflammation. Individual genes (FDR <
- 3 0.05) are shown with log2 fold change alongside their gene set and corresponding GSEA
- 4 enrichment score.

- 6 Figure 6. L-sulforaphane as a potential selective histone deacetylase 8 inhibitor. Lung
- 7 sections stained with anti-acetylated histone (red) and anti-acetylated α-tubulin (green) show
- 8 strong staining in ovalbumin-L-sulforaphane (OVA-LSF) mice (A). Merged image: nucleus
- stained with DAPI (blue), acetylated histones H3 or H2B (red), acetylated α -tubulin (green).
- H2Bac was analyzed in both models (B); H3ac and acetylated α -tubulin analyzed in the
- prevention model (C). Histone deacetylase (HDAC) 8 expression investigated in the prevention
- model of chronic allergic airways disease (AAD) (D). LSF reduces the enzymatic activity of
- 13 HDAC8; $EC_{50} = 92.07 \pm 7.45 \,\mu\text{M}$ (SAHA $EC_{50} = 306 \,\text{nM}$ in the same assay) (E). Data
- represented as the mean \pm SEM; *p<0.05 **p<0.01 and ***p<0.001. Western blot shows 15 μ M
- LSF decreases HDAC8 expression and increases acetylated α-tubulin and H3ac in A549 lung
- cells (positive control = 10µM SAHA) (F). Molecular docking of LSF to HDAC8 (G). Aligned
- structures of HDAC8, for PDB ID: 1T64 (1 pocket, green); 1T67 (2 pockets, red) and 1VKG (1
- groove, purple). Black sphere represents Zn. Viewed along axis parallel (Gi) and perpendicular
- to helix bundle (Gii). LSF binding sites to HDAC8, 1 pocket (green), 2 pockets (purple) and 1
- 20 groove (red). Helix-loop B-helix motif highlighted in black. Viewed along axis parallel (Giii)
- and perpendicular to helix bundle (Giv). Predicted binding pose of LSF to the tertiary-deep sub-
- 22 site of 1 pocket of HDAC8. Residues 21-49 are shown in ribbon representation. HDAC
- 23 sidechains in contact with LSF are shown in bonds representation (Gv). The tertiary-deep sub-

site (green) is predicted for all three HDAC8 structures. The tertiary-interm sub-site (purple) is predicted for the 1 pocket and 2 pockets structures. The tertiary-shallow sub-site (red) is only predicted for the 1 groove structure. Residues 21-49 are shown in opaque grey ribbon representation (Gvi). Potential steric clash between the residue 21-31 (HDAC8 numbering) helix region of HDAC3 (grey ribbon) and LSF (green spheres). The corresponding helix HDAC8 (red ribbon) is shown for comparison. Sequence alignment between HDAC3 and HDAC8 shows the extra two residues present for the former isoform compared to the latter are partially responsible for occlusion of the tertiary site (Gvii). Figure 7. Mechanisms associated with the attenuation of ovalbumin-induced allergic airways disease by L-sulforaphane. Summary of the changes that occur to normal bronchioles in the ovalbumin (OVA)-induced chronic murine model of allergic airways disease (AAD) as observed in this study. The mechanisms associated with prevention and reversal of the pathobiology by L-sulforaphane (LSF) are depicted; antioxidant, anti-inflammatory and epigenetic mechanisms of action are shown. Methodologies used to detect changes are in indicated in brackets; FL = immunofluorescence.

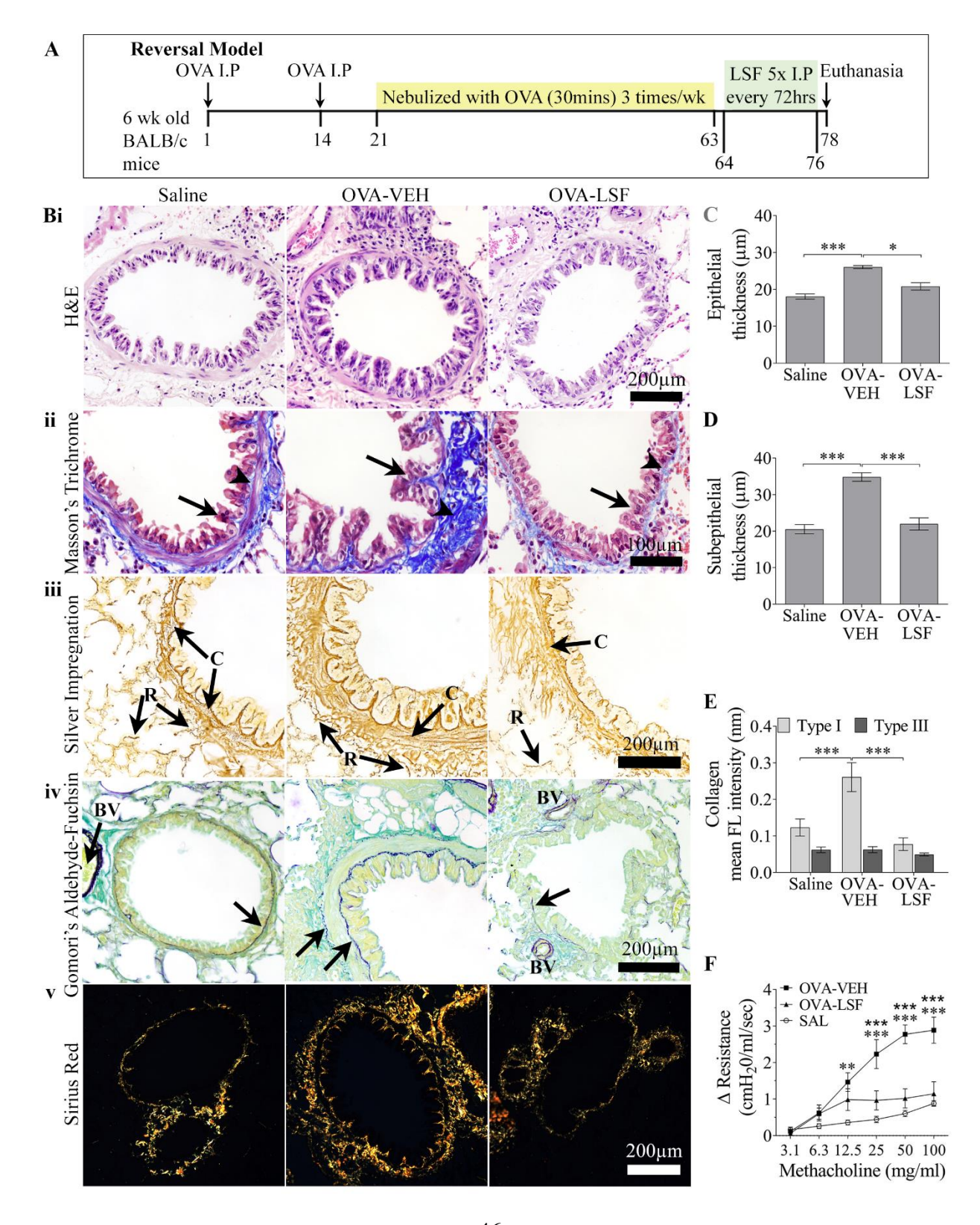
1 Figure 1. L-sulforaphane protects from bronchial mucosal damage in a murine chronic

2 model of allergic airways disease.

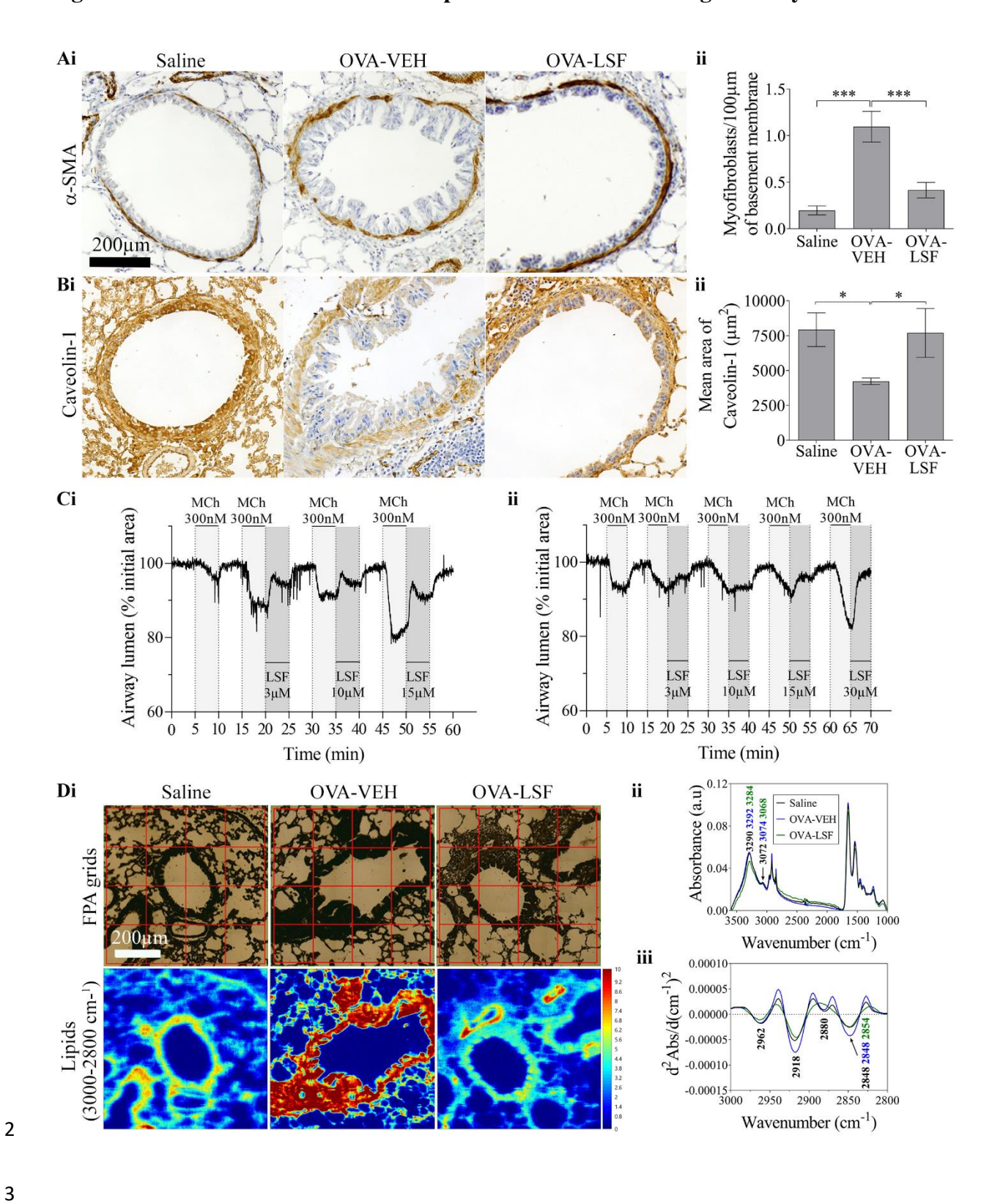


1 Figure 2. L-sulforaphane reverses bronchial remodeling in a murine model of chronic

2 allergic airways disease.

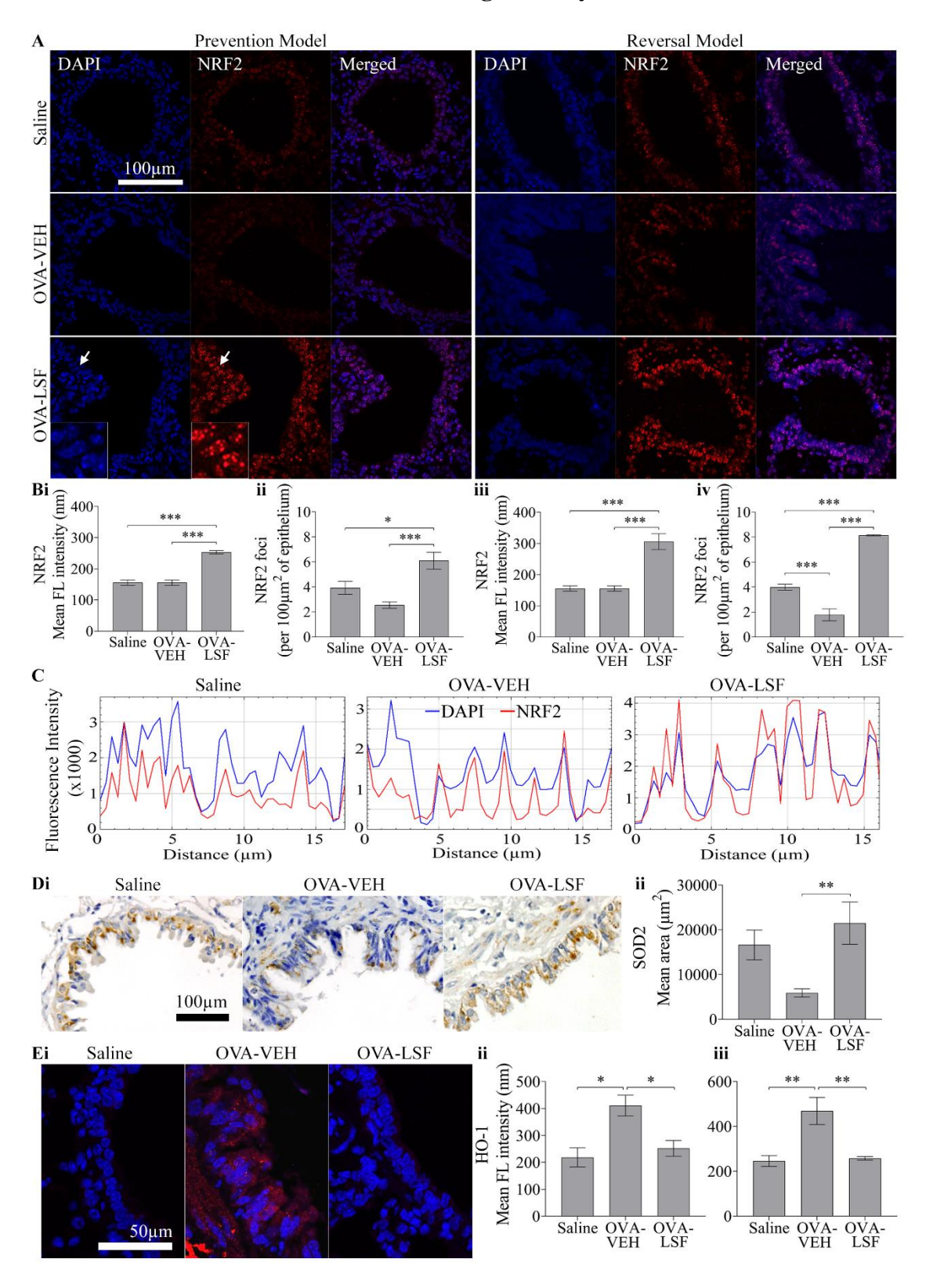


1 Figure 3. Molecular effects of L-sulforaphane in the chronic allergic airways disease model.



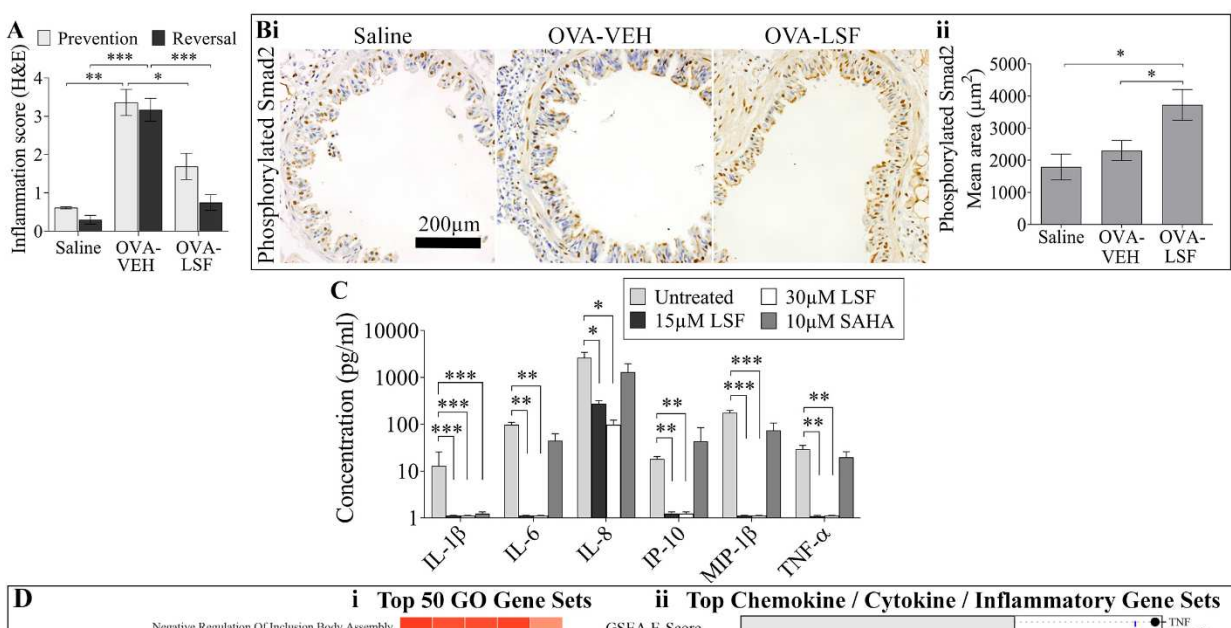
1 Figure 4. L-sulforaphane modulates key antioxidant defense pathways in both the

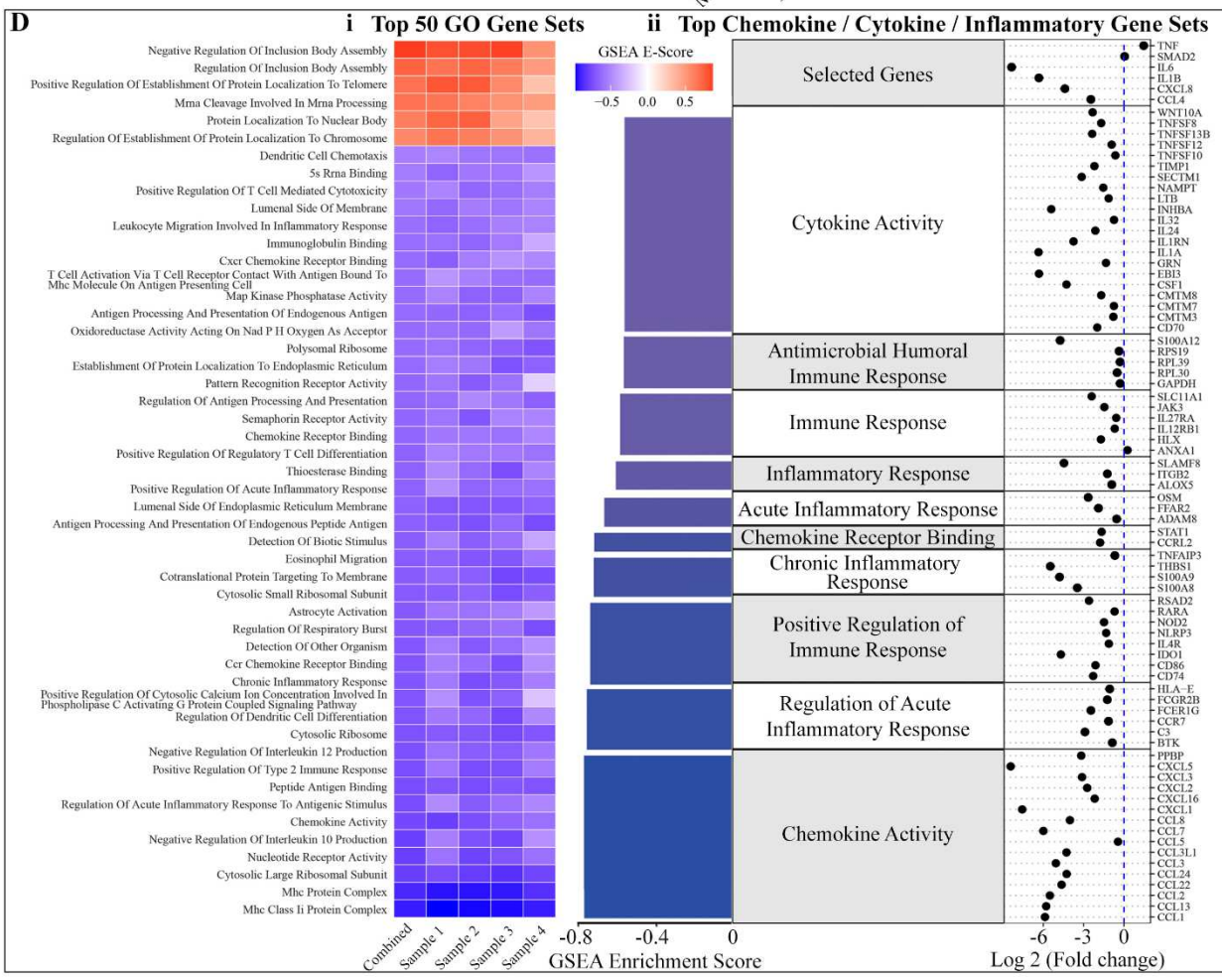
2 prevention and reversal model of chronic allergic airways disease.



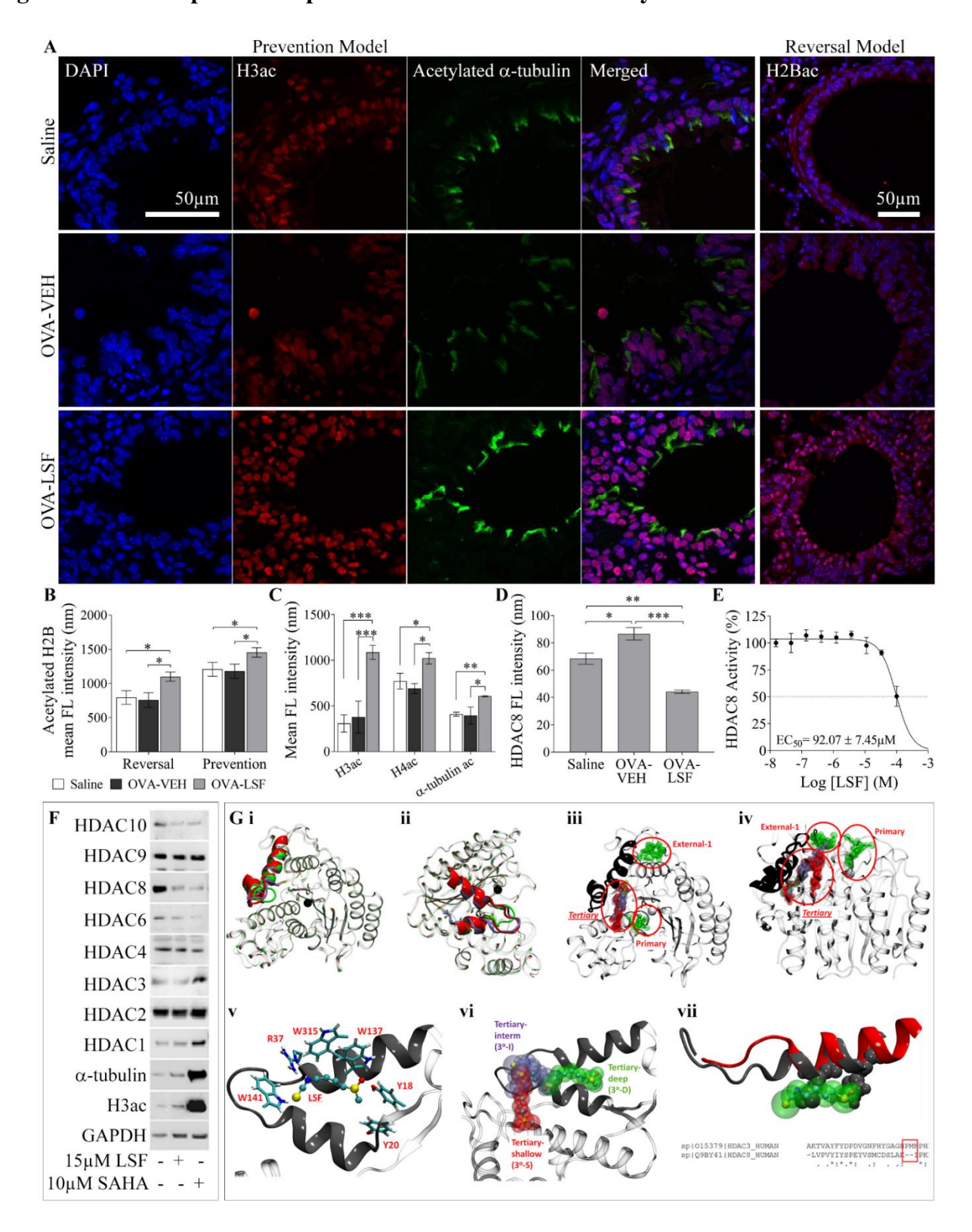
1 Figure 5. L-sulforaphane reduces inflammation via down-regulation of pro-inflammatory

2 genes.



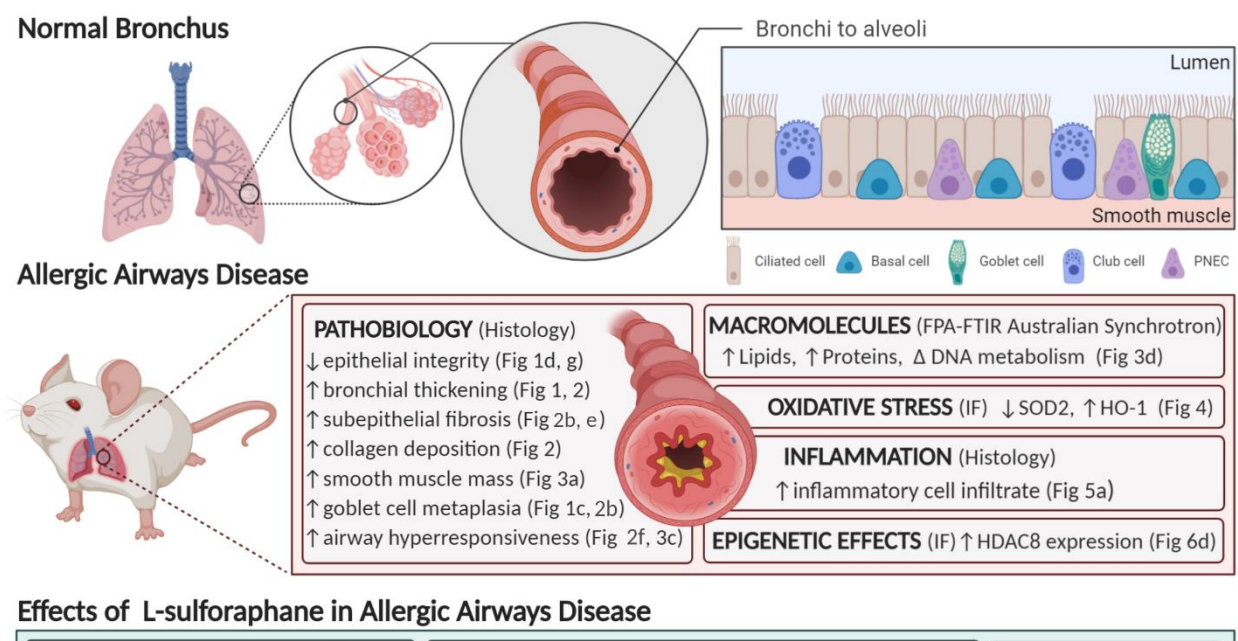


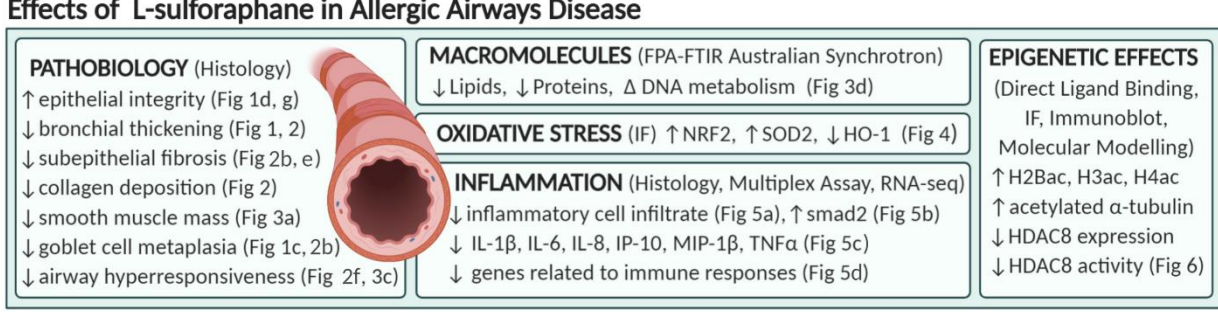
1 Figure 6. L-sulforaphane as a potential selective histone deacetylase 8 inhibitor.



1 Figure 7. Mechanisms associated with the attenuation of ovalbumin-induced allergic

2 airways disease by L-sulforaphane.





- 1 Acknowledgments: We acknowledge the intellectual and financial support from McCord
- 2 Research (Iowa, USA). The authors would like to acknowledge the use of the facilities provided
- 3 by Monash University (Clayton, VIC, Australia) and the Murdoch Children's Research Institute
- 4 (Parkville, VIC, Australia) for their care and husbandry of the mice. The Gomori's aldehyde-
- 5 fuchsin and silver impregnation stains were performed by Ms Laura Leone at the Melbourne
- 6 University Histology Platform (University of Melbourne, School of Biomedical Sciences,
- 7 Parkville, VIC, Australia). The authors would like to acknowledge the use of the facilities
- 8 provided by Monash Micro Imaging (MMI) at the Alfred Research Alliance (ARA, Melbourne,
- 9 VIC, Australia) and particularly, the expert assistance from Drs Stephen Cody and Iśka
- 10 Carmichael. FPA-FTIR imaging measurements were undertaken at the IRM beamline at the
- Australian Synchrotron, part of ANSTO (Clayton, VIC, Australia). Various figures in this
- manuscript were created with BioRender.com. We thank the National Computing Infrastructure
- 13 (NCI), and the Pawsey Supercomputing Centre in Australia (funded by the Australian
- 14 Government). Further, we thank the Spartan High Performance Computing service (University
- of Melbourne), and the Partnership for Advanced Computing in Europe (PRACE) for awarding
- the access to Piz Daint, hosted at the Swiss National Supercomputing Centre (CSCS),
- 17 Switzerland. We acknowledge our use of the gene set enrichment analysis, GSEA software, and
- 18 Molecular Signature Database (MSigDB) (Subramanian, Tamayo, et al. (2005), PNAS 102,
- 19 15545-15550, http://www.broad.mit.edu/gsea/).

- Funding: We would like to acknowledge intellectual and financial support by McCord Research
- 22 (Iowa, USA). AEO is supported by an National Health and Medical Research Council
- 23 (NHMRC) Senior Research Fellowship (1154650). PVL is supported by an NHMRC Career

- 1 Development Fellowship (1146198). CD is supported by an NHMRC Early Career Postdoctoral
- 2 Fellowship (1120152). JL is supported by an Australian Government Research Training Program
- 3 Scholarship.

- 5 **Author contributions:** SGR, JEB, MEC, AH, PVL, CSS, KJS, MLKT, AE, and TCK
- 6 conceptualized the ideas and overarching aims. JEB, MEC, AH, PVL, CSS, KJS, MJT, JV,
- 7 MLKT, AE, and TCK were involved in supervision. KV, CD, AH, IK, JL, SM, NM, EP, MJT,
- 8 JV, and MZ participated in the development and design of the methodology. KV, CD, IK, SM,
- 9 NM, MJT, JV, and MZ conducted the research and investigation process. RCB, AH, JL, EP, and
- MZ were responsible for visualization and KV, EP, SGR, PVL, and TCK were involved in
- production of the first draft of the manuscript.

12

- 13 Competing interests: Epigenomic Medicine Program (TCK) was supported financially by
- McCord Research (Iowa, USA), which has a financial interest in dietary compounds including
- sulforaphane.
- 16 The remaining co-authors declare that they have no direct financial relation with the commercial
- identities mentioned in this manuscript that might lead to a conflict of interest.

- 19 Data and materials availability: RNA sequencing data is available from GEO under the
- accession GSE160353. To review GEO accession GSE160353 while it remains in private status,
- 21 go the following address and enter the access token: otmlcuoillwhicd
- 22 https://www.ncbi.nlm.nih.gov/geo/query/acc.cgi?acc=GSE160353